



ELSEVIER

Contents lists available at SciVerse ScienceDirect

Journal of Computational Physics

journal homepage: www.elsevier.com/locate/jcp

A matched interface and boundary method for solving multi-flow Navier–Stokes equations with applications to geodynamics

Y.C. Zhou ^{a,*}, Jianguo Liu ^a, Dennis L. Harry ^b

^a Department of Mathematics, Colorado State University, Fort Collins, CO 80523-1874, USA

^b Department of Geosciences, Warner College of Natural Resources, Colorado State University, Ft Collins, CO 80523-1874, USA

ARTICLE INFO

Article history:

Received 19 February 2011

Received in revised form 16 July 2011

Accepted 8 September 2011

Available online 17 September 2011

Keywords:

Navier–Stokes equations

Geophysics

Multi-flow

Jump conditions

Interface method

Non-staggered grid

Projection method

Stability

ABSTRACT

We have developed a second-order numerical method, based on the matched interface and boundary (MIB) approach, to solve the Navier–Stokes equations with discontinuous viscosity and density on non-staggered Cartesian grids. We have derived for the first time the interface conditions for the intermediate velocity field and the pressure potential function that are introduced in the projection method. Differentiation of the velocity components on stencils across the interface is aided by the coupled fictitious velocity values, whose representations are solved by using the coupled velocity interface conditions. These fictitious values and the non-staggered grid allow a convenient and accurate approximation of the pressure and potential jump conditions. A compact finite difference method was adopted to explicitly compute the pressure derivatives at regular nodes to avoid the pressure–velocity decoupling. Numerical experiments verified the desired accuracy of the numerical method. Applications to geophysical problems demonstrated that the sharp pressure jumps on the elast–Newtonian matrix are accurately captured for various shear conditions, moderate viscosity contrasts and a wide range of density contrasts. We showed that large transfer errors will be introduced to the jumps of the pressure and the potential function in case of a large absolute difference of the viscosity across the interface; these errors will cause simulations to become unstable.

© 2011 Elsevier Inc. All rights reserved.

1. Introduction

This paper proposes a novel numerical method for solving the Navier–Stokes equations describing multi-flows, i.e., flows with distinct density and viscosity in subdomains of the flow field. Our study is motivated by the need to simulate highly viscous creeping flows that model a wide variety of geodynamic processes; these processes usually involve viscous, non-Newtonian visco-elastic, viscoplastic, or visco-elasto-plastic rheologies [2,6,19,30,32,37,39,51,54]. Of particular interest is the convection in Earth's mantle that occurs at depths ranging from about 100 km to 2900 km [7,21,33,40,61]. The rocks within Earth's mantle behave visco-plastically over geologic time scales (thousands to millions of years), and behave elasto-plastically over time scales associated with the earthquake cycle and seismic wave propagation (seconds to hundreds of years). The strength of mantle rocks varies with depth, with the elastic and viscous behaviors being different. The elastic moduli increase monotonically with depth, due primarily to the increasing pressure, with the shear modulus ranging approximately from 60 to 300 GPa and the bulk modulus ranging from about 100 to 600 GPa [1,9,15]. The viscous behavior is more complicated, with the viscosity decreasing with the depth above about 660 km. Below 660 km, there are conflicting

* Corresponding author.

E-mail address: yzhou@math.colostate.edu (Y.C. Zhou).

models, some advocating a stepwise monotonic increase in the viscosity with depth [1] and some advocating a maximum viscosity located within the middle of the lower mantle [58]. It is generally agreed, however, that mantle viscosities range from 10^{18} to 10^{23} Pa s [37,38]. The pressure within the mantle varies from about 2 to 150 GPa and the density varies from 3100 to 5500 kg/m³, both increasing with depth. Pressure-induced phase changes occur within the transition zone that separates the upper and lower mantle, between 660 and 900 km depth, making the changes in pressure, density, viscosity, and elastic moduli stepwise continuous within this interval. A dramatic change in earth properties occurs at the interface between the mantle and the outer core (approximately 2900 km depth). Here, the vertical derivative of the bulk modulus approximately doubles, the shear modulus drops to zero within the outer core, density increases by a factor of two, and viscosity decreases by 25 orders of magnitude [1,9,15].

Modeling mantle Stokes flow with these sharp viscosity contrasts (within the transition zone and at the core-mantle boundary) and over these wide ranges of viscosities poses challenges to geophysicists and mathematicians. In most geodynamically relevant cases this difficulty is further complicated by the need to track moving interfaces between different subdomains within the mantle (for example, upwelling plumes of geochemically or thermally distinct material). Standard numerical methods such as finite difference (FD), finite volume (FV), finite element (FE) and spectral methods have a long history of applications in modeling the mantle convection, as summarized in [60]. Recently, a number of specialized techniques have been developed to capture the sharp variation of viscosity across model domain boundaries. These include a multi-grid method [28], an adaptive multilevel wavelet collocation method [52], a hybrid spectral/finite difference method [41], and a finite element method with Q2P1 basis functions [42]. Some of these methods have been implemented in popular software for computational geophysics, such as GANGO [20], Gale [14], and CitCom [29,47]. However, many of these numerical methods do not have a sufficiently high resolution to resolve the sharp viscosity contrasts (which often occur over the width of a few numerical grid points) adequately to obtain accurate solutions. This is particularly a problem if a mesh element is cut by the material interface. A recent comprehensive study [8] shows that the quality of the solutions from either finite difference methods or finite element methods depends critically on the averaging technique used to define the viscosity at the interface elements, and on the type of mesh for finite element methods. The accuracy of the pressure solution appears more sensitive to the definition of the viscosity in numerical grids, and in some cases its error can be two orders of magnitude greater than the error in velocity. The convergence of the numerical solution is found slow except for the case where the material interface is perfectly fitting the mesh. These observations motivate us to introduce jumps of velocity, pressure and their derivatives induced by the discontinuous viscosity and density into the numerical simulations of the mantle convection on regular Cartesian grid. We anticipate that this novel numerical approach will not only improve the accuracy of the solution of the tectonic stress, but will also help save time for dynamically generating an interface-fitting numerical grid when the approach is combined with level set, volume-of-fluid (VOF) or other interface tracking techniques.

Solving fluid flow with an internal interface using finite difference methods on the regular Cartesian grid was first proposed by Peskin in simulating the blood flow through different valves in the heart [35]. The heart wall and valves interfacing atria and ventricles are described as elastic membranes with vanishing thickness moving with the fluid particles next to them. The forces exerted by the membranes to the blood flow are therefore singular in nature, and are spread to the grid points nearby through appropriately represented discrete delta functions. Immersed boundary methods are widely used in simulating fluid–solid interactions in biology fluid dynamics [36], including the most recent simulations of molecular motor proteins, microtubules and other subcellular organelles [3]. Instead of smoothing out the singular forces, the ghost flow method defines ghost points to carry the flow variables of the other fluid at the grid points physically occupied by a fluid. The jump conditions for the velocity and pressure at the interface are utilized to define the flow variables at the ghost points [12,13]. In many applications the variables of a real fluid are directly taken as the ghost variables if these variables are continuous across the interface, while the ghost values of the discontinuous variables are usually computed via extrapolation. These treatments limit the accuracy of the numerical approximation to the first order because a continuous variable of the flow field may have discontinuous derivatives at the interface. Third-order approximations to the interface conditions are constructed in the immersed interface method (IIM) by LeVeque and Li [23]. In IIM methods proper terms are devised to correct the standard central difference schemes for discretizing the derivatives near the interface so that a globally second-order solution can be obtained. The appealing mathematical features and many promising applications of the IIM methods to various types of differential equations are well documented by Li and Ito [24]. In addition to these and many other finite difference methods based on the Cartesian grid [53,59,63,62], finite volume methods and finite elements methods are developed to solve the interface problems on unstructured grids that are not necessarily conforming to the internal interface [25,11,27,16,34,17]. Specialized basis functions are needed to represent the kinks or the jumps of the solutions on the interface elements. Progress has been made in designing basis functions satisfying the interface conditions for solving single elliptical or parabolic equation, but much needs to be done to solve systems of differential equations with coupled interface conditions, for example, the Navier–Stokes equations.

The formulations and implementability of interface conditions of the Navier–Stokes equations differ significantly depending on the nature of the fluid flow. If the interface conditions are induced by the singular force exerted by the internal membrane, jumps of the velocity components and pressure are decoupled and can be given as functions of the force on the membrane only [26]. See [56] also for a systematic derivation of interface conditions for Navier–Stokes equations and [22] for the computation of the singular force and the consistent jumps of the velocity and pressure using a spline interpolation. For flows with distinct viscosities or densities in different subdomains, the continuity conditions for the viscous stress on the interface couple the velocity and pressure, and thus pose substantial difficulty for their numerical implementation

[18]. It was found that the jump conditions for the velocity and pressure can also be related to the velocity on the interface and its tangential derivatives if the viscosity is discontinuous but the density is not. This makes it possible to introduce an augmented velocity at selected control points on the interface to provide a convenient evaluation of jump conditions for the velocity and pressure [49,48]. Appropriate iterations are needed to ensure the convergence of the augmented velocity on the interface along with all other field variables. If both the viscosity and density are discontinuous, the mixed derivative of the augmented velocity will appear in the interface conditions for the pressure [55]. This challenges the applications of the augmented velocity method, and new techniques are expected.

The current study is focused on solving the Navier–Stokes equation with large viscosity and density contrasts at fixed material interface. Our interface method is based on the matched interface and boundary (MIB) approach that was originally developed for solving elliptical interface problems [63,62] on the standard Cartesian grid. The MIB method manages to obtain a highly accurate discretization of the derivatives by using fictitious points that represent the smooth extension of the flow field from the other side of the interface. The values at the fictitious points are computed by *implicitly* enforcing the interface conditions to a designed order of accuracy. The low order interface conditions can be repeatedly used with increasingly larger stencils to accommodate a discretization of order four or higher. These fictitious values enable us to directly compute the velocity and its partial derivatives at the intersections of the interface and the grid lines, and to compute the pressure jump conditions at the same intersections without resorting to the augmented velocity field because of the use of a non-staggered grid. We find that the errors in the approximate derivatives of the velocity at the interface will be amplified into the jump conditions of pressure in case of large difference of viscosity or large difference of viscosity/density ratio across the interface, and this might explain the numerical instability encountered in the current study and that in [49]. The time integration of the unsteady Navier–Stokes equations is accomplished by using a second-order projection method, in which a potential function ϕ is defined by a Poisson equation for updating the pressure and correcting the velocity. This Poisson equation has the reciprocal of the fluid density as its coefficient, and therefore constitutes an elliptical interface problem if the density is discontinuous, as considered in this study. This interface problem is not completely addressed in [18], where it is simply discretized using the standard central differencing. The Poisson equation in [49,48] has a discontinuous fluid viscosity as the coefficient, and thus also deserves special numerical treatments. It is worth noting that the intermediate velocity and the potential function are introduced purely for the numerical purpose; there are no underlying physical interface conditions for them. In this study we derive for these two variables the interface conditions that are consistent with the true velocity, pressure and the projection method.

The rest of the article is organized as follows. In Section 2 we introduce the model of incompressible Navier–Stokes equations with a piecewise constant viscosity and a piecewise constant density. We then summarize the interface conditions for the velocity, pressure and the potential function in the context of the projection method. Approximations to these coupled interface conditions using the MIB approach are described in Section 3, where the details of implementation are also presented. Numerical experiments and the applications to two model geodynamic problems admitting analytical solutions are discussed in Section 4. We make conclusions and remarks in Section 5.

2. Multi-flow Navier–Stokes equations and interface conditions

We consider a rectangular domain $\Omega \in \mathbb{R}^2$ filled with two viscous fluids with distinct viscosities and densities. The boundary of Ω is denoted by $\partial\Omega$ and the interface separating the two fluids is denoted by Γ . The two subdomains are denoted by Ω_1 and Ω_2 , and the viscosity and density are μ_1, ρ_1 and μ_2, ρ_2 in the subdomains Ω_1 and Ω_2 , respectively, c.f. Fig. 1 for an illustration. We allow that $\partial\Omega \cap \Gamma \neq \emptyset$, i.e., the interface can intersect the boundary; the resulting sharp-edged intersections can be treated by using the techniques presented below in conjunction with the special techniques developed in [57]. The full time-dependent incompressible Navier–Stokes equations are

$$\nabla \cdot \mathbf{u} = 0, \tag{1}$$

$$\rho(\mathbf{u}_t + (\mathbf{u} \cdot \nabla)\mathbf{u}) = -\nabla p + (\nabla \cdot \boldsymbol{\tau})^T + \mathbf{F} + \rho\mathbf{g}, \tag{2}$$

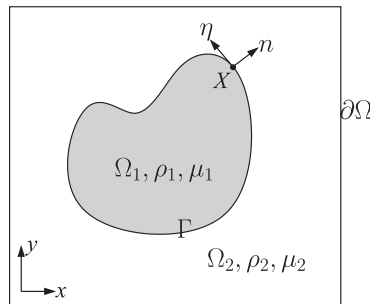


Fig. 1. Illustration of the computational domain for multi-flow problems.

where $\mathbf{u} = (u, v)$ is the velocity vector, ρ is the mass density, p is the pressure, \mathbf{F} is the force applied only on the interface (surface tension excluded), \mathbf{g} is the gravitational acceleration vector, the superscript T denotes the matrix transpose, and

$$\boldsymbol{\tau} = \mu(\nabla\mathbf{u} + \nabla\mathbf{u}^T) = \mu \begin{pmatrix} 2u_x & u_y + v_x \\ u_y + v_x & 2v_y \end{pmatrix} \quad (3)$$

is the viscous stress tensor. Here the subscripts t and x, y denote the partial derivatives with respect to the referred variables. Let the arc length parametrization of the interface Γ be $\mathbf{X}(s, t)$, the singular force \mathbf{F} will be given by the surface force density \mathbf{f} by

$$\mathbf{F}(\mathbf{x}, t) = \int_{\Gamma} \mathbf{f}(s, t) \delta(\mathbf{x} - \mathbf{X}(s, t)) ds, \quad (4)$$

where s is the arc-length and δ is the Dirac delta function. Let the unit normal of Γ be $\mathbf{n} = (n_1, n_2)$ pointing from Ω_1 to Ω_2 and the tangent vectors be $\boldsymbol{\eta} = (\eta_1, \eta_2)$. The jump conditions on Γ are given by

$$\left[\begin{pmatrix} \mathbf{n} \\ \boldsymbol{\eta} \end{pmatrix} (p\mathbf{I} - \boldsymbol{\tau}) \mathbf{n}^T \right] = \begin{pmatrix} \sigma\kappa + f_n \\ f_\eta \end{pmatrix}, \quad (5)$$

where \mathbf{I} is the identity matrix. These conditions describe that the normal stresses on the two sides of the interface with a curvature κ are balanced by the surface tension with the coefficient σ and the singular force $\mathbf{f} = (f_n, f_\eta)$ on the interface. The surface tension is non-zero for general multi-phase flows, but usually assumes a value of 0 in geodynamic problems. Here and in the sequel $[\cdot]$ denotes the jump of enclosed quantity across the interface. Using the definition of the stress tensor $\boldsymbol{\tau}$ we can write Eq. (5) as two separate conditions

$$[p - 2\mu(u_n, v_n) \cdot \mathbf{n}] = \sigma\kappa + f_n, \quad (6)$$

$$[\mu(u_n, v_n) \cdot \boldsymbol{\eta} + \mu(u_\eta, v_\eta) \cdot \mathbf{n}] = f_\eta, \quad (7)$$

Since the flow is viscous, the velocity field is continuous at the interface and thus

$$[u] = 0, \quad [v] = 0. \quad (8)$$

Consequently,

$$[u_\eta] = 0, \quad [v_\eta] = 0. \quad (9)$$

Considering the divergent-free condition on two sides of the interface in the local coordinate system

$$\mathbf{0} = \nabla \cdot \mathbf{u} = (u_n, v_n) \cdot \mathbf{n} + (u_\eta, v_\eta) \cdot \boldsymbol{\eta}, \quad (10)$$

we obtain

$$[(u_n, v_n) \cdot \mathbf{n}] = 0. \quad (11)$$

This suggests that the quantity

$$D \stackrel{\text{def}}{=} (u_n, v_n) \cdot \mathbf{n} \quad (12)$$

is continuous across the interface, and allows one to write the interface condition (6) as

$$[p] = 2[\mu]D + \sigma\kappa + f_n. \quad (13)$$

Moreover one can take the material derivative of $[\mathbf{u}] = 0$ to get

$$\mathbf{0} = \frac{\partial[\mathbf{u}]}{\partial t} + (\mathbf{u} \cdot \nabla)[\mathbf{u}] = \mathbf{0}.$$

This suggests that

$$\left[-\frac{\nabla p}{\rho} + \frac{(\nabla \cdot \boldsymbol{\tau})^T}{\rho} + \mathbf{F} + \mathbf{g} \right] = \mathbf{0},$$

and thus give rises to the following interface conditions for the two partial derivatives of the pressure:

$$\begin{aligned} \left[\frac{p_x}{\rho} \right] &= \left[\frac{2(\mu u_x)_x + (\mu(u_y + v_x))_y}{\rho} \right] + f_x, \\ \left[\frac{p_y}{\rho} \right] &= \left[\frac{(\mu(u_y + v_x))_y + 2(\mu v_y)_y}{\rho} \right] + f_y, \end{aligned}$$

whereby we consider the fact that the gravitational field \mathbf{g} is continuous on Ω . The forces f_x, f_y are the representations of f_n, f_η in the local coordinate. For divergence-free flows with piecewise constant viscosity these are equivalent to

$$\begin{bmatrix} p_x \\ \rho \end{bmatrix} = \begin{bmatrix} \mu \Delta u \\ \rho \end{bmatrix} + f_x, \quad \begin{bmatrix} p_y \\ \rho \end{bmatrix} = \begin{bmatrix} \mu \Delta v \\ \rho \end{bmatrix} + f_y. \tag{14}$$

Remark 2.1. In [18] alternative combinations of velocity interface conditions are derived from the essential conditions (6)–(10). The essential condition Eq. (10) also allows other combinations, e.g., $[\mu(u_n, v_n) \cdot \mathbf{n}] = 0$.

If viscosity is discontinuous but density is continuous, it was shown that the jump conditions for the velocity, pressure and their first-order derivatives depend only on the interface velocity and its derivatives [48,49]. Thus for 2D problems one can first compute the interface velocity $\mathbf{v} \stackrel{\text{def}}{=} \mathbf{u}(\Gamma)$, named augmented variables, at selected control points on the interface and then use 1D interpolations along the interface to approximate the velocity and its tangential derivatives at arbitrary points on the interface. Two prominent advantages of the augmented variable approach are (i) the interface conditions for velocity components are decoupled, and thus each component can be integrated independently; and (ii) the augmented variables on the interface allow interpolation and differentiation at arbitrary points on the interface. The approach therefore works nicely with the staggered-grid where the interface conditions for the velocity and pressure are applied at different positions. The jump conditions for the second-order derivatives of the velocity, nevertheless, cannot be computed only from the augmented velocity, because

$$\left[\mu \frac{\partial^2 \mathbf{u}}{\partial n \partial \eta} \right] = [\mu] \kappa \frac{\partial \mathbf{v}}{\partial \eta} + \frac{d}{d\eta} \left[\mu \frac{\partial \mathbf{u}}{\partial n} \right]. \tag{15}$$

If viscosity and density are both discontinuous, the jump conditions of the normal derivative of the pressure can be written as

$$\begin{aligned} \left[\frac{1}{\rho} \frac{\partial p}{\partial n} \right] &= \left[\frac{\mu}{\rho} \mathbf{n} \cdot \Delta \mathbf{u} \right] = - \left[\frac{\mu}{\rho} \mathbf{n} \cdot \nabla \times \boldsymbol{\omega} \right] = \frac{d}{d\eta} \left(\boldsymbol{\tau} \cdot \left[\frac{\mu}{\rho} \boldsymbol{\omega} \times \mathbf{n} \right] \right) = \frac{d}{d\eta} \left(\boldsymbol{\tau} \cdot \left[\frac{\mu}{\rho} \frac{\partial \mathbf{u}}{\partial \mathbf{n}} \right] - \left[\frac{\mu}{\rho} \right] \left(\frac{\partial \mathbf{v}}{\partial \eta} \cdot \mathbf{n} \right) \right) \\ &= \kappa \mathbf{n} \cdot \left[\frac{\mu}{\rho} \frac{\partial \mathbf{u}}{\partial \mathbf{n}} \right] + \eta \cdot \frac{d}{d\eta} \left[\frac{\mu}{\rho} \frac{\partial \mathbf{u}}{\partial \mathbf{n}} \right] + \left[\frac{\mu}{\rho} \right] \kappa \eta \cdot \frac{\partial \mathbf{v}}{\partial \eta} - \left[\frac{\mu}{\rho} \right] \mathbf{n} \cdot \frac{\partial^2 \mathbf{v}}{\partial \eta^2}, \end{aligned} \tag{16}$$

where $\boldsymbol{\omega} = \nabla \times \mathbf{u}$ is the vorticity, and the identities

$$\Delta \mathbf{u} = -\nabla \times \boldsymbol{\omega} + \nabla(\nabla \cdot \mathbf{u}), \quad \boldsymbol{\omega} \times \mathbf{n} = \frac{\partial \mathbf{u}}{\partial \mathbf{n}} - (\nabla \mathbf{u}) \cdot \mathbf{n}$$

are used. This representation of the pressure interface condition also involves the normal derivative of the velocity on the interface. Furthermore, generalization of the augmented variable approach to 3D Navier–Stokes equations and use of spline interpolation on the unstructured control points over the interface, which is now a 2D surface, could be very challenging. For these reasons we choose not to interpolate from the velocities at the control points but to use the fictitious velocity values to directly compute the interface conditions for pressure at the intersections of interface and grid lines. We will adopt the primitive form of the coupled interface conditions for velocity, i.e., Eqs. (6)–(10), to solve all components of the velocity at the same time. We choose Eq. (14) rather than Eq. (16) as the first-order interface conditions of the pressure because the former combination decouples the jump relations in coordinate directions and thus is easier to implement.

2.1. Projection method and interface conditions for the intermediate velocity and the pressure potential

We use a second-order projection method to integrate the Navier–Stokes equations and to enforce the divergence-free condition. Let the time increment be Δt and assume that the solutions are known up to $t = t_k$, an intermediate velocity field \mathbf{u}^* is first solved from

$$\frac{\mathbf{u}^* - \mathbf{u}^k}{\Delta t} + (\mathbf{u} \cdot \nabla \mathbf{u})^{k+1/2} = -\frac{1}{\rho} \nabla p^{k-1/2} + \frac{\mu}{2\rho} (\Delta \mathbf{u}^* + \Delta \mathbf{u}^k) + \mathbf{g}, \tag{17}$$

where the nonlinear advection term is extrapolated from the two previous steps through

$$(\mathbf{u} \cdot \nabla \mathbf{u})^{k+1/2} = \frac{3}{2} (\mathbf{u}^k \cdot \nabla \mathbf{u}^k) - \frac{1}{2} (\mathbf{u}^{k-1} \cdot \nabla \mathbf{u}^{k-1}). \tag{18}$$

A scalar potential ϕ is defined by the Poisson equation

$$\nabla \cdot \left(\frac{\nabla \phi}{\rho} \right) = \frac{\nabla \cdot \mathbf{u}^*}{\Delta t}. \tag{19}$$

The velocity and the pressure at the new time step are then computed by

$$\mathbf{u}^{k+1} = \mathbf{u}^* - \frac{\Delta t}{\rho} \nabla \phi, \tag{20}$$

$$p^{k+1/2} = p^{k-1/2} + \phi - \frac{\mu}{2\rho} \nabla \cdot \mathbf{u}^*. \tag{21}$$

Limited by the regularity of \mathbf{u} and p , the intermediate velocity \mathbf{u}^* and potential ϕ will have singularities of certain degree at the interface. Hence we need to prescribe proper interface conditions that shall be enforced in the numerical approximation of their derivatives. We first equip the velocity field \mathbf{u}^* with the same type of all the essential interface conditions as \mathbf{u} :

$$[\mathbf{u}_\eta^*] = [\mathbf{v}_\eta^*] = 0, \quad (22)$$

$$[\mu(\mathbf{u}_n^*, \mathbf{v}_n^*) \cdot \boldsymbol{\eta} + \mu(\mathbf{u}_\eta^*, \mathbf{v}_\eta^*) \cdot \mathbf{n}] = f_\eta, \quad (23)$$

$$\nabla \cdot \mathbf{u}^* = (\mathbf{u}_n^*, \mathbf{v}_n^*) \cdot \mathbf{n} + (\mathbf{u}_\eta^*, \mathbf{v}_\eta^*) \cdot \boldsymbol{\eta} = 0. \quad (24)$$

In other words, we enforce the intermediate velocity field on the interface to be continuous, have the same continuity of the viscous stress tensor, and be divergence free there, although \mathbf{u}^* may have non-vanishing divergence in $\Omega \setminus \Gamma$. We then prescribe the interface conditions of ϕ such that they are compatible with the interface conditions of \mathbf{u} and \mathbf{u}^* . Indeed Eq. (20) indicates that

$$\left[\frac{\nabla \phi}{\rho} \right] = [\mathbf{u}^*] - [\mathbf{u}^{k+1}] = 0, \quad (25)$$

since both \mathbf{u}^* and \mathbf{u}^{k+1} are continuous on the interface. Furthermore, Eq. (21) suggests that

$$[\phi] = [p^{k+1/2}] - [p^{k-1/2}] + \left[\frac{\mu}{2\rho} \nabla \cdot \mathbf{u}^* \right] = [p^{k+1/2}] - [p^{k-1/2}], \quad (26)$$

noticing that \mathbf{u}^* has been prescribed to be divergence-free at the interface. Consequently we need to compute $[p^{k-1/2}]$ and $[p^{k+1/2}]$ to approximate $[\phi]$ needed for solving the Poisson equation (19). Ideally the jump $[p^{k+1/2}]$ shall be computed from Eq. (13) with $D^{k+1/2} = (\mathbf{u}_n^{k+1/2}, \mathbf{v}_n^{k+1/2}) \cdot \mathbf{n}$. This seems difficult because \mathbf{u}^{k+1} is not available when $p^{k+1/2}$ is needed. We then consider the same extrapolation as Eq. (18) to approximate

$$D^{k+1/2} = \frac{3}{2}D^k - \frac{1}{2}D^{k-1}, \quad (27)$$

suggesting that

$$[p^{k+1/2}] = [\mu](3D^k - D^{k-1}) + \sigma\kappa + f_n. \quad (28)$$

To compute $[p^{k-1/2}]$, we need $D^{k-1/2}$, which can be approximated by interpolation because the velocities at t_k and t_{k-1} are known:

$$D^{k-1/2} = \frac{1}{2}(D^k + D^{k-1}). \quad (29)$$

With these we can compute

$$[\phi] = [p^{k+1/2}] - [p^{k-1/2}] = 2[\mu](D^{k+1/2} - D^{k-1/2}) = [\mu](D^k - D^{k-1}). \quad (30)$$

Remark 2.2. An iterative procedure is designed in [49] to ensure the velocity and pressure to have consistent interface conditions at each time step. In that study the density is continuous but the Poisson equation for ϕ has a discontinuous viscosity μ as the coefficient. Although the interface conditions for ϕ are not explicitly addressed, there shall exist a jump of ϕ at the interface as indicated by Eq. (26), regardless of the regularity of the density when the viscosity is discontinuous.

Remark 2.3. The intermediate velocity field \mathbf{u}^* is available when solving the Poisson equation (19) for ϕ . Eq. (17) indicates that $\mathbf{u}^* = \mathbf{u}^{n+1} + \mathcal{O}(\Delta t^2)$ because $\nabla p^{n+1/2} = \nabla p^{1-1/2} + \mathcal{O}(\Delta t)$ [4]. It appears plausible to use this \mathbf{u}^* instead \mathbf{u}^{n+1} to compute $[p^{k+1/2}]$. We then consider the following approximation to $[\phi]$ as an alternative to Eq. (30):

$$[\phi] = [p^{k+1/2}] - [p^{k-1/2}] = 2[\mu] \left(\frac{D^* + D^k}{2} - \frac{D^k + D^{k-1}}{2} \right) = [\mu](D^* - D^{k-1}). \quad (31)$$

3. Computational algorithms

We consider the discretization of the 2D Navier–Stokes equations on a non-staggered grid, where the pressure and velocity components are defined at the same set of grid points. As a result, one can conveniently compute the partial derivatives of the velocity at the intersections of the interface and the grid lines, where the interface conditions of pressure are needed. In contrast, on a staggered grid the grid lines for the velocity and pressure fields intersect the interface at different points, and this makes it difficult to compute the jumps of pressure and its derivatives at the interface from the velocity field. However, special treatments are necessary for the non-staggered grids to prevent the grid-scale oscillations of the pressure that are

caused by the even–odd decoupling of the pressure and velocity fields. In this study we manage to introduce $p_{i,j}$ into the approximation of $\frac{\partial p}{\partial x}(i,j)$ and $\frac{\partial p}{\partial y}(i,j)$ by using a compact difference scheme. The compact scheme is applied only to the regular nodes. The approximation of the derivatives of p at an irregular node (i,j) always involves $p_{i,j}$ by the construction of the fictitious values. This approach to obtaining pressure–velocity coupling is similar to a recent implementation in [5]. The approximation of the interface conditions of velocity and pressure will be described below. We follow the convention to use the superscripts +, – to denote the variables on the two sides of the interface.

3.1. Matching interface conditions of velocity

We will approximate the two zero-order interface conditions

$$[u] = 0, \quad [v] = 0, \tag{32}$$

and the two first-order interface conditions

$$[(u_n, v_n) \cdot n] = 0, \quad [\mu(u_n, v_n) \cdot \eta + \mu(u_\eta, v_\eta) \cdot n] = f_\eta. \tag{33}$$

The tangential derivatives of $[u] = 0, [v] = 0$ and the divergence–free conditions on the two sides of the interface will be used during the approximations. With the MIB method we will reduce the dimensionality of the interface conditions and solve the fictitious values along each coordinate direction [63]. To approximate the coupled interface conditions of the velocity, we define fictitious velocity at nodes (i,j) and $(i+1,j)$ if the interface intersects the grid line at a point between these two nodes, c.f. Fig. 2(a). These two fictitious values allow us to approximate u^\pm, v^\pm and u_x^\pm, v_x^\pm . Some of the partial derivatives with respect to y have to be approximated with the help of auxiliary points. We work with the essential interface conditions to reduce the number of y -derivatives to be approximated. If the local arrangement of the grid points and the interface supports the interpolations of auxiliary points for approximating u_y^\pm, v_y^\pm , we shall retain these two partial derivatives by applying the two substitutions

$$v_y^- = -u_x^-, \quad u_y^- = (u_x^+ - u_x^-) \frac{\eta_1}{\eta_2} + u_y^+,$$

in Eq. (33). This gives

$$\begin{pmatrix} 1 & 2\mu^+n_1\eta_1 - \mu^- \frac{\eta_1}{\eta_2}(n_2\eta_1 + n_1\eta_2) \\ -n_1^2 & 4\mu^-n_1n_2 + \mu^- \frac{\eta_1}{\eta_2}(n_2\eta_1 + n_1\eta_2) \\ n_1n_2 & \mu^+(n_1\eta_2 + n_2\eta_1) \\ -n_2n_2 & -\mu^-(n_1\eta_2 + n_2\eta_1) \\ 0 & [\mu](n_1\eta_2 + n_2\eta_1) \\ n_2^2 & 2\mu^+n_2\eta_2 \end{pmatrix} \mathbf{P} = \begin{pmatrix} 0 \\ f_\eta \end{pmatrix}, \tag{34}$$

where $n = (n_1, n_2), \eta = (\eta_1, \eta_2)$ and $\mathbf{P} = (u_x^+, u_x^-, v_x^+, v_x^-, u_y^+, v_y^+)^T$. If (u_y^-, v_y^-) instead of (u_y^+, v_y^+) are chosen to be approximated, we can use

$$v_y^+ = -u_x^+, \quad u_y^+ = -(u_x^+ - u_x^-) \frac{\eta_1}{\eta_2} + u_y^-,$$

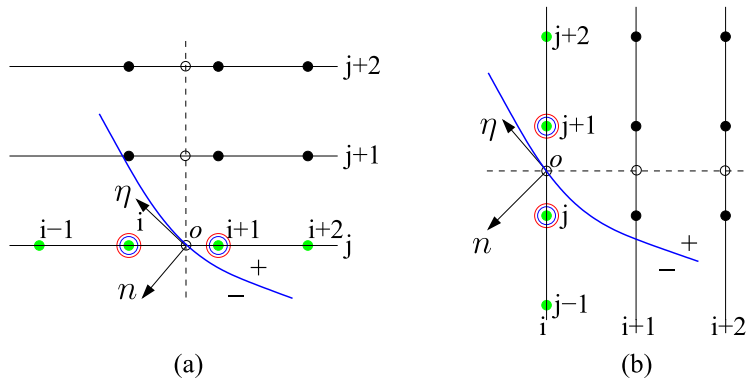


Fig. 2. (a) Definition of fictitious values $f_{i,j}, f_{i+1,j}$ (red circles) for u and $g_{i,j}, g_{i+1,j}$ (blue circles) at $(i,j), (i+1,j)$, respectively. Partial derivatives u_y^\pm, v_y^\pm are approximated by using the values at the auxiliary nodes (black circles) on the auxiliary line (dash). (b) Definition of fictitious values $f_{i,j}, f_{i,j+1}$ (red circles) for u and $g_{i,j}, g_{i,j+1}$ (blue circles) at $(i,j), (i,j+1)$, respectively. Partial derivatives u_x^\pm, v_x^\pm are approximated by using the values at the auxiliary nodes (black circles) on the auxiliary line (dash). (For interpretation of the references to color in this figure legend, the reader is referred to the web version of this article.)

to get the combination

$$\begin{pmatrix} n_1^2 & -4\mu^+ n_1 n_2 - \mu^+ \frac{\eta_1}{\eta_2} (n_2 \eta_1 + n_1 \eta_2) \\ -1 & -2\mu^- n_1 \eta_1 + \mu^+ \frac{\eta_1}{\eta_2} (n_2 \eta_1 + n_1 \eta_2) \\ n_1 n_2 & \mu^+ (n_1 \eta_2 + n_2 \eta_1) \\ -n_1 n_2 & -\mu^- (n_1 \eta_2 + n_2 \eta_1) \\ 0 & [\mu] (n_2 \eta_1 + n_1 \eta_2) \\ -n_2^2 & -2\mu^- n_2 \eta_2 \end{pmatrix}^T \mathbf{P} = \begin{pmatrix} 0 \\ f_\eta \end{pmatrix} \tag{35}$$

with $\mathbf{P} = (u_x^+, u_x^-, v_x^+, v_x^-, u_y^-, v_y^-, v_y^+)^T$. These two combinations assume that $\eta_2 \neq 0$, but $\eta_2 = 0$ can hold true for very special cases as shown in Fig. 3. Fig. 3(a) illustrates that the two nodes $(i, j), (i + 1, j)$ are on the same side of the interface, and thus no fictitious values are needed for discretizing x -partial derivatives of the velocity or pressure at these two nodes. The fictitious values at nodes $(i, j), (i - 1, j)$ in Fig. 3(b) can be solved along the y direction following the algorithms described below.

Fictitious values of u, v at irregular nodes $(i, j), (i, j + 1)$ are needed for discretizing the y -derivatives if the y -grid line at x_i intersects the interface at a point between these two nodes, as shown in Fig. 2(b). To solve for these fictitious values we need jump conditions for u_y, v_y , which can be derived by eliminating some of the x -derivatives in the essential interface conditions. If approximations of u_x^+, v_x^+ are preferred, one can eliminate u_x^-, v_x^- through

$$u_x^- = -v_y^-, \quad v_x^- = v_x^+ + (v_y^+ - v_y^-) \frac{\eta_2}{\eta_1},$$

to get

$$\begin{pmatrix} n_1 n_2 & 2\mu^+ n_1 \eta_1 \\ -n_2 n_2 & [\mu] (n_1 \eta_2 + n_2 \eta_1) \\ 1 & \mu^+ (n_2 \eta_1 + n_1 \eta_2) \\ -n_2^2 & -\mu^- (n_2 \eta_1 + n_1 \eta_2) \\ n_1^2 & 2\mu^+ n_2 \eta_2 - \mu^- \frac{\eta_2}{\eta_1} (n_1 \eta_2 + n_2 \eta_1) \\ 0 & -4\mu^- n_1 n_2 + \mu^- \frac{\eta_2}{\eta_1} (n_1 \eta_2 + n_2 \eta_1) \end{pmatrix}^T \mathbf{P} = \begin{pmatrix} 0 \\ f_\eta \end{pmatrix}, \tag{36}$$

where $\mathbf{P} = (u_x^+, v_x^+, u_y^+, u_y^-, v_y^+, v_y^-)^T$. If u_x^-, v_x^- are chosen to be approximated we use

$$u_x^+ = -v_y^+, \quad v_x^+ = (v_y^+ - v_y^-) \frac{\eta_2}{\eta_1},$$

to eliminate of u_x^+, v_x^+ and get

$$\begin{pmatrix} n_1 n_2 & -2\mu^- n_1 \eta_1 \\ -n_1 n_2 & [\mu] (n_1 \eta_2 + n_2 \eta_1) \\ n_2^2 & \mu^+ (n_2 \eta_1 + n_1 \eta_2) \\ -1 & -\mu^- (n_2 \eta_1 + n_1 \eta_2) \\ -n_1^2 & 4\mu^+ n_1 n_2 - \mu^+ \frac{\eta_2}{\eta_1} (n_1 \eta_2 + n_2 \eta_1) \\ 0 & -2\mu^- n_2 \eta_2 + \mu^+ \frac{\eta_2}{\eta_1} (n_1 \eta_2 + n_2 \eta_1) \end{pmatrix}^T \mathbf{P} = \begin{pmatrix} 0 \\ f_\eta \end{pmatrix} \tag{37}$$

now with $\mathbf{P} = (u_x^-, v_x^-, u_y^+, u_y^-, v_y^+, v_y^-)^T$. Here we assume that $\eta_1 \neq 0$, while the cases with $\eta_1 = 0$ can be treated as discussed above.

We may encounter situations where the interface intersects a grid line right at a node (i, j) , as shown in Fig. 4. If $n_1 n_2 \neq 0$ we will retain all first-order derivatives in the essential interface conditions to get the following combination:

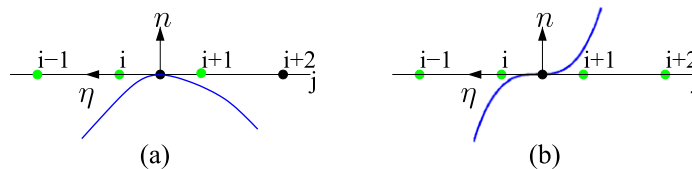


Fig. 3. Two examples illustrating $\eta_2 = 0$ at the intersection of the interface and the grid line. (a) Nodes (i, j) and $(i + 1, j)$ are on the same side of the interface. (b) Fictitious values at the nodes $(i, j), (i + 1, j)$ cannot be solved along x -direction but can be solved along y -direction.

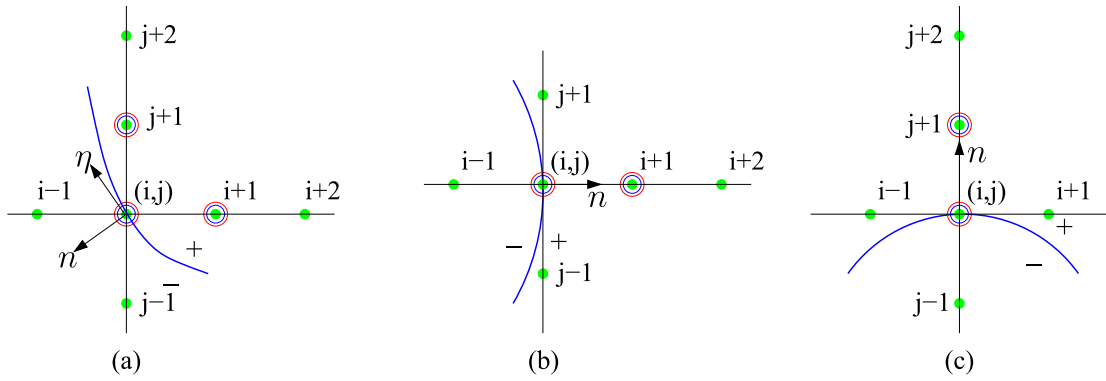


Fig. 4. Interface intersects the grid line at node (i, j) with (a) $n_1 n_2 \neq 0$; (b) $n_2 = 0$; and (c) $n_1 = 0$. Decoupled interface conditions can be derived for cases (b) and (c).

$$\begin{pmatrix} \eta_1 & 0 & 2\mu^+ n_1 \eta_1 & n_1^2 \\ -\eta_1 & 0 & -2\mu^- n_1 \eta_1 & -n_1^2 \\ 0 & \eta_1 & \mu^+(n_1 \eta_2 + n_2 \eta_1) & n_1 n_2 \\ 0 & -\eta_1 & -\mu^-(n_1 \eta_2 + n_2 \eta_1) & -n_1 n_2 \\ \eta_2 & 0 & \mu^+(n_1 \eta_2 + n_2 \eta_1) & n_1 n_2 \\ -\eta_2 & 0 & -\mu^-(n_1 \eta_2 + n_2 \eta_1) & -n_1 n_2 \\ 0 & \eta_2 & 2\mu^+ n_2 \eta_2 & n_2^2 \\ 0 & -\eta_2 & -2\mu^- n_2 \eta_2 & -n_2^2 \end{pmatrix}^T \mathbf{P} = \begin{pmatrix} 0 \\ 0 \\ f_\eta \\ 0 \end{pmatrix}, \tag{38}$$

where $\mathbf{P} = (u_x^+, u_x^-, v_x^+, v_x^-, u_y^+, u_y^-, v_y^+, v_y^-)^T$. If $n_1 n_2 = 0$ at the intersection as shown in Fig. 4(b) and (c), the solution of fictitious values are decoupled. Indeed, in Fig. 4(b) where $n_2 = 0$ we notice that $[v_y] = [v_\eta] = 0$ and therefore the two conditions in Eq. (33) can be simplified to yield two conditions

$$[u] = 0, \quad [u_x] = 0 \tag{39}$$

for solving fictitious values $f_{i,j}$, $f_{i+1,j}$, and the other two conditions

$$[v] = 0, \quad [\mu v_x] = [\mu] u_y \tag{40}$$

for solving fictitious values $g_{i,j}$, $g_{i+1,j}$. These solutions can be obtained by following the 1D MIB method [63], noticing that u_y can be approximated on either side of the interface because $[u_y] = [u_\eta] = 0$ in this case. Similar simplifications will lead to the jump conditions

$$[v] = 0, \quad [v_y] = 0 \tag{41}$$

for solving fictitious values $g_{i,j}$, g_{i+1} , and the jump conditions

$$[u] = 0, \quad [\mu u_y] = [\mu] v_x \tag{42}$$

for solving fictitious values $f_{i,j}$, f_{i+1} .

We now proceed to solve the four fictitious values, (f_i, g_i) for (u, v) at the node (i, j) and the fictitious values (f_{i+1}, g_{i+1}) for (u, v) at the node $(i + 1, j)$, simultaneously from

$$[u] = 0, \quad [v] = 0$$

and one of the combinations Eqs. (34) and (35). We illustrate a complete solution procedure for the case shown in Fig. 2(a), for which the condition Eq. (34) is used. The transposed matrix in Eq. (34) will be denoted by $\mathbf{M} = \{M_{ij}\}$ for simplicity. The velocity components u, v and their partial derivatives with respect to x will be approximated with the aid of the fictitious values, while u_x^+, v_x^+ at the interface will be approximated by using auxiliary nodes, i.e.,

$$u^- = \sum_{l=i-1}^i P_{0,l}^- u_{l,j} + P_{0,i+1}^- f_{i+1,j}, \quad u^+ = P_{0,i}^+ f_{i,j} + \sum_{l=i+1}^{i+2} P_{0,l}^+ u_{l,j}, \tag{43}$$

$$v^- = \sum_{l=i-1}^i P_{0,l}^- v_{l,j} + P_{0,i+1}^- g_{i+1,j}, \quad v^+ = P_{0,i}^+ g_{i,j} + \sum_{l=i+1}^{i+2} P_{0,l}^+ v_{l,j}, \tag{44}$$

$$u_x^- = \sum_{l=i-1}^i P_{1,l}^- u_{l,j} + P_{1,i+1}^- f_{i+1,j}, \quad u_x^+ = P_{1,i}^+ f_{i,j} + \sum_{l=i+1}^{i+2} P_{1,l}^+ u_{l,j}, \tag{45}$$

$$v_x^- = \sum_{l=i-1}^i P_{1,l}^- v_{l,j} + P_{1,i+1}^- g_{i+1,j}, \quad v_x^+ = P_{1,i}^+ g_{i,j} + \sum_{l=i+1}^{i+2} P_{1,l}^+ v_{l,j}. \tag{46}$$

where $P_{0,l}^\pm$ is the weight at the node (l,j) of the 1D Lagrange interpolant of $u^\pm(x,y)$ at the point (x_0,y_0) , and $P_{1,l}^\pm$ is the weight at the node (l,j) of the finite difference approximation to $u_x^\pm(x_0,y_0)$. We define auxiliary values $u_1^0, u_2^0, v_1^0, v_2^0$ and use a one-sided finite difference with weights $\{W_l\}_{l=0}^2$ to approximate the y -derivatives:

$$u_y^+ = W_0 u_0 + \sum_{l=1}^2 W_l u_l^0, \quad v_y^+ = W_0 v_0 + \sum_{l=1}^2 W_l v_l^0. \tag{47}$$

Equating $u_0 = u^-$ and representing the fictitious values in terms of \mathbf{V} defined by

$$\mathbf{V} = (u_{i-1,j}, u_{i,j}, u_{i+1,j}, u_{i+2,j}, u_1^0, u_2^0, v_{i-1,j}, v_{i,j}, v_{i+1,j}, v_{i+2,j}, v_1^0, v_2^0, f_\eta)^T$$

such that

$$f_{i,j} = \mathbf{C}_1 \cdot \mathbf{V}, \quad f_{i+1,j} = \mathbf{C}_2 \cdot \mathbf{V}, \quad g_{i,j} = \mathbf{C}_3 \cdot \mathbf{V}, \quad g_{i+1,j} = \mathbf{C}_4 \cdot \mathbf{V},$$

we can summarize the approximation to the four interface conditions as

$$\mathcal{M} \begin{pmatrix} \mathbf{C}_1 \\ \mathbf{C}_2 \\ \mathbf{C}_3 \\ \mathbf{C}_4 \end{pmatrix} \mathbf{V} = \mathbf{E}. \tag{48}$$

Here

$$\mathcal{M} = \begin{pmatrix} P_{0,i}^+ & -P_{0,i+1}^- & 0 & 0 \\ 0 & 0 & P_{0,i}^+ & -P_{0,i+1}^- \\ M_{12}P_{1,i}^+ & (M_{11} + M_{15}W_0)P_{1,i+1}^- & M_{14}P_{1,i}^+ & (M_{13} + M_{16}W_0)P_{1,i+1}^- \\ M_{22}P_{1,i}^+ & (M_{21} + M_{25}W_0)P_{1,i+1}^- & M_{24}P_{1,i}^+ & (M_{23} + M_{26}W_0)P_{1,i+1}^- \end{pmatrix},$$

and

$$\begin{aligned} E_1 &= \sum_{l=i-1}^i P_{0,l}^- u_{l,j} - \sum_{l=i+1}^{i+2} P_{0,l}^+ u_{l,j}, & E_2 &= \sum_{l=i-1}^i P_{0,l}^- v_{l,j} - \sum_{l=i+1}^{i+2} P_{0,l}^+ v_{l,j}, \\ E_3 &= - \sum_{l=i-1}^i P_{1,l}^- (M_{11} + M_{15}W_0) u_{l,j} - \sum_{l=i-1}^i P_{1,l}^- (M_{13} + M_{16}W_0) v_{l,j} \\ &\quad - \sum_{l=i+1}^{i+2} P_{1,l}^+ (M_{12} u_{l,j} + M_{14} v_{l,j}) - M_{15} \sum_{l=1}^2 W_l u_l^0 - M_{16} \sum_{l=1}^2 W_l v_l^0, \\ E_4 &= - \sum_{l=i-1}^i P_{1,l}^- (M_{21} + M_{25}W_0) u_{l,j} - \sum_{l=i-1}^i P_{1,l}^- (M_{23} + M_{26}W_0) v_{l,j} \\ &\quad - \sum_{l=i+1}^{i+2} P_{1,l}^+ (M_{22} u_{l,j} + M_{24} v_{l,j}) - M_{25} \sum_{l=1}^2 W_l u_l^0 - M_{26} \sum_{l=1}^2 W_l v_l^0 + f_\eta. \end{aligned}$$

Defining matrix \mathbf{B} such that $\mathbf{E} = \mathbf{B}\mathbf{V}$, we can readily solve for the four sets of expansion coefficients

$$\mathbf{C} = \mathcal{M}^{-1}\mathbf{B}.$$

The weights on the auxiliary points shall be further distributed over the nodes involved in the approximation to these two values. c.f. [62,63] for details. A linear system similar to (48) can be assembled for the other interface conditions (35) by simply replacing the two partial derivatives u_y^+, v_y^+ in (48) by u_y^-, v_y^- , respectively, keeping in mind that M_{ij} now refers to the entry of the matrix in Eq. (35). The procedure for solving fictitious values along y -grid lines is described in Appendix A.

Finally we describe the approximation of the interface conditions (38) for solving the fictitious values $f_{i+1,j}, f_{i+1,j}, g_{i+1,j}, g_{i+1,j}$ as shown in Fig. 4(a). The fictitious values $f_{i,j} = u_{i,j}, g_{i,j} = v_{i,j}$ follow directly from the continuity of the velocity. Applying the discretizations of all partial derivatives

$$\begin{aligned} u_x^- &= \sum_{l=i-1}^i P_{1,l}^- u_{l,j} + P_{1,i+1}^- f_{i+1,j}, & v_x^- &= \sum_{l=i-1}^i P_{1,l}^- v_{l,j} + P_{1,i+1}^- g_{i+1,j}, \\ u_y^- &= \sum_{l=j-1}^j Q_{1,l}^- u_{i,l} + Q_{1,j+1}^- f_{i,j+1}, & v_y^- &= \sum_{l=j-1}^j Q_{1,l}^- v_{i,l} + Q_{1,j+1}^- g_{i,j+1}, \end{aligned}$$

$$u_x^+ = \sum_{l=i}^{i+2} P_{1,l}^+ u_{lj}, v_x^+ = \sum_{l=i}^{i+2} P_{1,l}^+ v_{lj}, \quad u_y^+ = \sum_{l=j}^{j+2} Q_{1,l}^+ u_{il}, v_y^+ = \sum_{l=j}^{j+2} Q_{1,l}^+ v_{il},$$

and using the expansions

$$f_{i+1,j} = \mathbf{C}_1 \cdot \mathbf{V}, \quad f_{ij+1} = \mathbf{C}_2 \cdot \mathbf{V}, \quad g_{i+1,j} = \mathbf{C}_3 \cdot \mathbf{V}, \quad g_{ij+1} = \mathbf{C}_4 \cdot \mathbf{V}$$

with

$$\mathbf{V} = (u_{i-1,j}, u_{ij}, u_{i+1,j}, u_{i+2,j}, v_{i-1,j}, v_{ij}, v_{i+1,j}, v_{i+2,j}, f_{ij})^T,$$

one can derive from Eq. (38), whose transposed matrix denoted by \mathbf{M} , a linear system

$$\begin{pmatrix} M_{12}P_{1,i+1}^- & M_{16}Q_{1,j+1}^- & M_{14}P_{1,i+1}^- & M_{18}Q_{1,j+1}^- \\ M_{22}P_{1,i+1}^- & M_{26}Q_{1,j+1}^- & M_{24}P_{1,i+1}^- & M_{28}Q_{1,j+1}^- \\ M_{32}P_{1,i+1}^- & M_{36}Q_{1,j+1}^- & M_{34}P_{1,i+1}^- & M_{38}Q_{1,j+1}^- \\ M_{42}P_{1,i+1}^- & M_{46}Q_{1,j+1}^- & M_{44}P_{1,i+1}^- & M_{48}Q_{1,j+1}^- \end{pmatrix} \begin{pmatrix} \mathbf{C}_1 \\ \mathbf{C}_2 \\ \mathbf{C}_3 \\ \mathbf{C}_4 \end{pmatrix} \mathbf{V} = \mathbf{E}, \tag{49}$$

where

$$E_m = -M_{m1} \sum_{l=i}^{i+2} P_{1,l}^+ u_{lj} - \sum_{l=i-1}^i P_{1,l}^- (M_{m2} u_{lj} + M_{m4} v_{lj}) - \sum_{l=j-1}^j Q_{1,l}^- (M_{m6} u_{il} + M_{m8} v_{il}) + \delta_{m2} f_{ij}, \quad m = 1, 2, 3, 4,$$

and δ_{ij} is the Kronecker delta function. Representing $\mathbf{E} = \mathbf{B}\mathbf{V}$ again but with a new matrix \mathbf{B} we can solve the four sets of expansion coefficients from $\mathbf{C} = \mathcal{M}^{-1}\mathbf{B}$ where \mathcal{M} is the matrix in Eq. (49).

Coupled fictitious values of u, v will be used to discretize the partial derivatives of u^k, v^k and u^*, v^* in Eq. (17) by using standard central differencing. For example, u_x, v_x, u_{xx}, v_{xx} at the node (i, j) in Fig. 2(a) can be computed by

$$u_x = \frac{f_{i+1,j} - u_{i-1,j}}{2\Delta x}, \quad u_{xx} = \frac{f_{i+1,j} - 2u_{ij} + u_{i-1,j}}{(\Delta x)^2}, \tag{50}$$

$$v_x = \frac{g_{i+1,j} - v_{i-1,j}}{2\Delta x}, \quad v_{xx} = \frac{g_{i+1,j} - 2v_{ij} + v_{i-1,j}}{(\Delta x)^2}, \tag{51}$$

for uniform grid spacings Δx and Δy in x and y directions, respectively. Replacing u, v by known u^k, v^k then these four difference schemes explicitly compute the four derivatives. If $u = u^*, v = v^*$ are to be solved, these four equations give rise to modified difference schemes at the irregular node (i, j) ; the resultant linear system couples u^* and v^* . We solve the linear equations by using the bi-conjugate gradient method preconditioned with an incomplete LU decomposition.

3.2. Matching interface conditions of pressure and potential

The procedure for solving fictitious pressure values is simplified thanks to the independent jump conditions for p_x, p_y . Indeed, one can solve for fictitious values in a direction without resorting to the approximation of the partial derivatives in other directions. For instance, when the fictitious pressure values $h_{ij}, h_{i+1,j}$ are needed for discretizing p_x at irregular points (i, j) and $(i + 1, j)$, we observe the interface conditions

$$[p] = 2[\mu]D + \sigma\kappa + f_n, \quad \left[\frac{p_x}{\rho} \right] = \left[\frac{\mu\Delta u}{\rho} \right]. \tag{52}$$

When the fictitious pressure values $h_{ij}, h_{i,j+1}$ are needed for discretizing p_y at the irregular nodes $(i, j), (i, j + 1)$, we consider the other set of interface conditions

$$[p] = 2[\mu]D + \sigma\kappa + f_n, \quad \left[\frac{p_y}{\rho} \right] = \left[\frac{\mu\Delta v}{\rho} \right]. \tag{53}$$

Due to the application of a non-staggered grid, the interface conditions (52) are defined at the same point of intersection for solving fictitious velocity values $f_{ij}, f_{i+1,j}$, c.f. Fig. 2(a). To compute D for a given velocity field \mathbf{u} , we need to compute u_x, u_y, v_x, v_y at the point of intersection O on the same side of the interface because $[D] = 0$. For convenience we choose the subdomain of Ω in which u_x, v_y are approximated in solving $f_{ij}, f_{i+1,j}$; this suggests Ω^+ will be chosen for the illustrated case. Two x -derivatives u_x^+, v_x^+ are to be approximated by using the equations in (45), (46), with fictitious values f_{ij}, g_{ij} replaced by their expansions. The y -derivatives are approximated by using Eq. (47). Similarly we can compute D in interface conditions (53) at the intersection (x_0, y_0) in Fig. 2(b).

After these jumps are computed, a detailed 1D procedure for solving h_{ij} and $h_{i+1,j}$ can be found in [63]. Solving fictitious potential values $\psi(i, j)$ and $\psi(i + 1, j)$ follow the same procedure as well, because the potential ϕ has the same type of uncoupled first-order interface conditions for ϕ_x, ϕ_y as the pressure p .

4. Numerical experiments and geophysical applications

In this section we first examine the accuracy and stability of the proposed algorithms for solving time-dependent Navier–Stokes equations. We then apply the algorithms to two geodynamic problems: a circular inclusion problem and an elliptical inclusion problem. Both are described by steady-state Stokes problems and admit analytical solutions.

4.1. A model problem

We adopt the unsteady circular flow problem in [49], which has a circular interface of radius $r_c = 0.5$ centered at $(0, 0)$. The flow field is given by

$$u(x, y, t) = \begin{cases} (1 - e^{-t})\left(\frac{y}{r} - 2y\right), & r > r_c, \\ 0, & r \leq r_c, \end{cases} \tag{54}$$

$$v(x, y, t) = \begin{cases} (1 - e^{-t})\left(-\frac{x}{r} + 2x\right), & r > r_c, \\ 0, & r \leq r_c, \end{cases} \tag{55}$$

$$p(x, y, t) = \begin{cases} \sin(\pi x) \sin(\pi y), & r > r_c, \\ 0, & r \leq r_c, \end{cases} \tag{56}$$

where $r = \sqrt{x^2 + y^2}$. This velocity field satisfies all the essential interface conditions (7)–(9) and (11) with $f_\eta = (1 - e^{-t})/r_c$. We choose the computational domain to be a square of $[-1, 1] \times [-1, 1]$, and solve the Navier–Stokes equations using time increment $\Delta t = \Delta x/10$ to $t = 2$. Noticing that projection method adopted here has a convergence rate of 2 in time for velocity and a rate of 1 for pressure [4], this chosen time increment ensures that the error due to the spatial discretization is dominant. The numerical errors are summarized in Table 1, which demonstrates that solutions of the velocity and pressure converge at an asymptotic rate about 2.

4.2. Circular inclusion problem

This problem describes a homogeneous clast of radius $r_c = 0.5$ embedded in a homogeneous matrix, the latter is subjected to a combined pure and shear stress on its exterior boundary, c.f. Fig. 5. This problem has application to a variety of geodynamic problems, including convection near the interface between the Earths mantle and core [58], differential rotation between the Earths inner and outer core [46], and grain scale deformation in shear zones in which stronger grains rotate quasi-rigidly within a viscous matrix [43,44]. The processes operate on a wide range of spatial scales, from hundreds of kilometers (mantle and core deformation) to millimeters (deformation in shear zones).

Table 1
Convergence tests of the circular flow problem. $\mu^+ = 10, \mu^- = 1, t = 2, \rho^+ = \rho^- = 1$.

$\Delta x = \Delta y$	$\ e_u\ _\infty$	Order	$\ e_p\ _\infty$	Order
1/10	3.6552E-3		8.7649E-3	
1/20	8.1930E-4	2.16	2.2500E-3	1.96
1/40	2.1483E-4	1.94	5.0953E-4	2.14
1/80	5.2278E-5	2.04	1.2674E-4	2.01

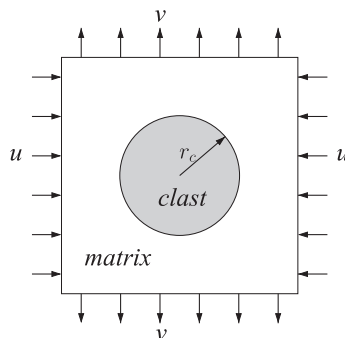


Fig. 5. Illustration of the circular inclusion problem.

In the polar coordinate (r, θ) with the origin located at the center of the clast, the following closed-form analytical solutions of the velocity and pressure can be derived by using the Muskhelishvili method [43]:

$$u_c = \frac{\mu_m}{\mu_m + \mu_c} (2\dot{\epsilon}x + \dot{\gamma}y) + \frac{1}{2} \dot{\gamma}y, \tag{57}$$

$$v_c = \frac{\mu_m}{\mu_m + \mu_c} (\dot{\gamma}x - 2\dot{\epsilon}y) - \frac{1}{2} \dot{\gamma}x, \tag{58}$$

$$u_m = \frac{1}{2} \dot{\gamma}y + \frac{1}{2} \left(r - \frac{\mu_c - \mu_m}{\mu_c + \mu_m} r_c^2 r^{-1} \right) (2\dot{\epsilon} \cos \theta + \dot{\gamma} \sin \theta) + \frac{1}{2} (r_c^4 r^{-3} - r_c^2 r^{-1}) \frac{\mu_c - \mu_m}{\mu_c + \mu_m} (2\dot{\epsilon} \cos 3\theta + \dot{\gamma} \sin 3\theta), \tag{59}$$

$$v_m = -\frac{1}{2} \dot{\gamma}x + \frac{1}{2} \left(r - \frac{\mu_c - \mu_m}{\mu_c + \mu_m} r_c^2 r^{-1} \right) (\dot{\gamma} \cos \theta - 2\dot{\epsilon} \sin \theta) + \frac{1}{2} (r_c^4 r^{-3} - r_c^2 r^{-1}) \frac{\mu_c - \mu_m}{\mu_c + \mu_m} (2\dot{\epsilon} \sin 3\theta - \dot{\gamma} \cos 3\theta), \tag{60}$$

$$p_c = 0, \tag{61}$$

$$p_m = -2Ar_c^2 r^{-2} (2\dot{\epsilon} \cos 2\theta + \dot{\gamma} \sin 2\theta), \tag{62}$$

where subscripts c and m denote the clast and the matrix, respectively, $\dot{\epsilon}$ is the pure stress rate, $\dot{\gamma}$ is the simple stress rate, and

$$A_c = \frac{\mu_m(\mu_c - \mu_m)}{\mu_c + \mu_m}.$$

It can be verified that the flow field satisfies the interface conditions (6)–(10). We choose the computational domain to be a $[-1, 1] \times [-1, 1]$ square, and obtain the steady-state solution by solving the time-dependent Stokes equations using $\Delta t = \Delta x / 10$ until the prescribed convergence threshold is met.

We first consider the flow field with a variable contrast of viscosity $r_\mu = \frac{\mu_c}{\mu_m}$ but with a constant density throughout the computational domain. We are particularly interested in the influence of viscosity contrast on the accuracy of the pressure solution, for which the convergence tests are summarized in Table 2. It is seen that the error in pressure increases significantly for large viscosity contrast; a similar instability found for large viscosity ratio is reported in [49]. Although the establishment of a rigorous analysis of this instability is not a focus of the current study, we speculate that this is caused by the approximation of the pressure jump conditions (13) and (14), where $[\mu]$ is the coefficient of D , and

$$\left[\frac{p_x}{\rho} \right] = \left[\frac{\mu \Delta u}{\rho} \right] = \begin{cases} \frac{1}{\rho} (\mu_c [\Delta u] + [\mu] \Delta u_m) \approx \frac{[\mu]}{\rho} \Delta u_m, & \text{if } \mu_m \gg \mu_c, \\ \frac{1}{\rho} (\mu_m [\Delta u] + [\mu] \Delta u_c) \approx -\frac{[\mu]}{\rho} \Delta u_c, & \text{if } \mu_c \gg \mu_m, \end{cases} \tag{63}$$

if $\Delta u_m \approx \Delta u_c$. A relation similar to (63) holds for $[p_y/\rho]$. It follows from this observation that the errors brought to D and $\Delta \mathbf{u}_{m,c}$ when they are computed from the numerical solution of \mathbf{u} will be amplified by a factor of $[\mu]$ and transferred into the approximate jump conditions for the pressure. Consequently when the viscosity difference is smaller than 1, the numerical error contained in \mathbf{u} and its derivatives will not be amplified, resulting the stable simulations as shown by the cases with $r_\mu = 10^{-3}$ and $r_\mu = 10^{-1}$ in Table 2. When that the viscosity difference is such that $[\mu] \gg 1$, the error carried by \mathbf{u} will be amplified significantly and brought into approximate pressure jumps, resulting in increasingly large errors as shown by the tests with $r_\mu = 10, 10^3$ in the table. Approximations of $[\phi]$ are subjected to the same magnitude of scaling of the numerical error, as seen in Eq. (25) or (31). Despite the larger errors, convergence is still achieved for these large viscosity differences.

As a numerical proof of this speculation we solve the Stokes equations for the four cases in Table 2 again, but with jump conditions of p, ϕ computed analytically. We note that such a treatment does not completely decouple the momentum equations and the pressure (potential) equation because $\nabla \cdot \mathbf{u}^*$ still appears in the source function of the Poisson equation for ϕ . Our convergence tests indicate that the numerical errors are nearly independent of the viscosity difference, hence only the results for $r_\mu = 1000$ are listed in Table 3. In Fig. 6 we plot the solution of \mathbf{u} interpolated at the intersections of the interface and the grid lines; values of D computed directly from the fictitious values are also plotted and compared to the analytical solutions. In the figure we also plot the D values computed by using a periodic cubic spline interpolation from the interpolated \mathbf{u} values at the interface/grid line intersections. It is observed that the D values computed through these two approaches have a comparable accuracy.

Table 2

Convergence tests of pressure solutions for the circular inclusion problem with fixed $\mu_m = 1, \rho_c = \rho_m = 1$ and the variable ratio $r_\mu = \mu_c/\mu_m$. All jumps in the interface conditions for p and ϕ are computed numerically.

$\Delta x = \Delta y$	$r_\mu = 10^{-3}$		$r_\mu = 10^{-1}$		$r_\mu = 10$		$r_\mu = 10^3$	
	$\ e_p\ _\infty$	Order	$\ e_p\ _\infty$	Order	$\ e_p\ _\infty$	Order	$\ e_p\ _\infty$	Order
1/10	4.50E-3		4.27E-3		1.15E-2		3.91E-1	
1/20	1.24E-3	1.86	1.12E-3	1.93	3.06E-3	1.91	1.21E-1	1.69
1/40	3.02E-4	1.62	3.44E-4	1.70	9.24E-4	1.73	3.07E-2	1.98
1/80	8.09E-5	1.81	8.63E-5	2.00	2.59E-4	1.81	9.88E-3	1.64

Table 3

Convergence tests of the pressure solution for the circular inclusion problem with $\rho_c = \rho_m = 1$ and $r_\mu = 1000$. Jump values in the interface conditions of p, ϕ are computed using the analytical solution.

$\Delta x = \Delta y$	1/10	1/20	1/40	1/80
$\ e_p\ _\infty$	2.01E-3	5.92E-4	1.67E-4	4.33E-5
Order		1.56	1.83	1.95

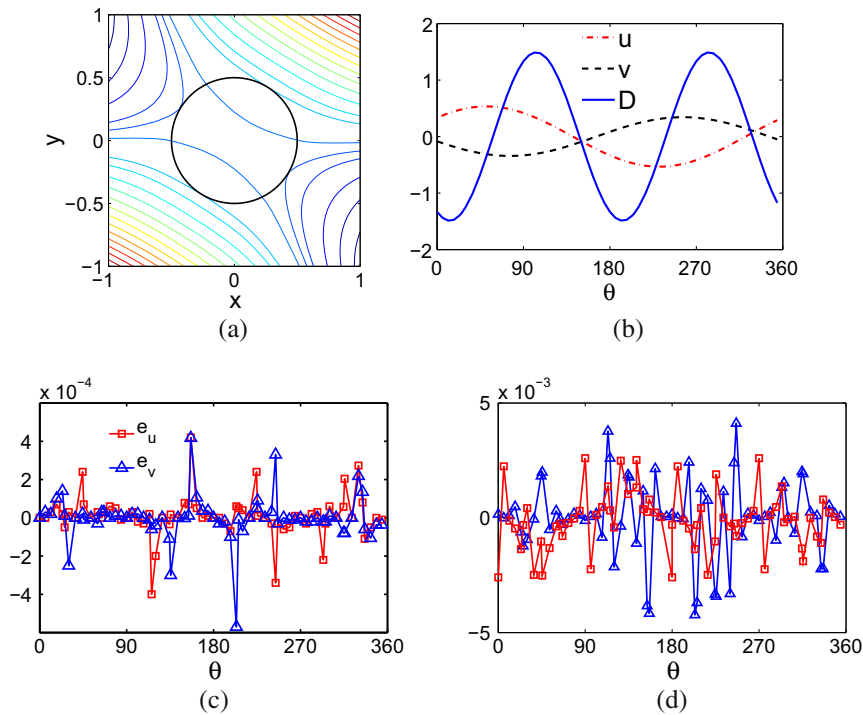


Fig. 6. (a) Stream function for the circular inclusion problem. (b) Computed velocity components and D values on the interface. (c) Errors of computed velocity components on the interface. (d) Errors of D on the interface. In (c) and (d) red squares denote the values computed from the interpolation or differentiation on the Cartesian grid using fictitious values, and blue triangles denotes the values computed from a cubic spline interpolation. (For interpretation of the references to color in this figure legend, the reader is referred to the web version of this article.)

We proceed to the numerical solutions of Stokes equations with discontinuous viscosity and density. Different from the viscosity contrast, density contrast in mantle flow is small in general. For instance, the density of the mantle is about 3370 kg/m^3 at a depth of 100 km, and is about 5566 kg/m^3 at a depth of 2891 km that is close to the half of the mean radius of the earth. We thus choose $\rho_m = 1$ and a range of $2 \leq \rho_c \leq 1000$ to cover most of the density contrasts of geodynamic relevance. The viscosities are fixed at $\mu_c = 10, \mu_m = 1$. Results of the convergence analysis are given in Table 4. A rate of convergence about 2 is obtained for all four density contrasts. Moreover, there is a slight decrease of the error with the increase of ρ_c . This decrease is the result of the reduced amplification of the error in the jumps of the first-order derivatives of p and ϕ . Indeed, at $\rho_c = 10$ we have

$$\begin{bmatrix} p_x \\ \rho \end{bmatrix} = \begin{bmatrix} \mu \Delta \mathbf{u} \\ \rho \end{bmatrix} = [\Delta \mathbf{u}],$$

Table 4

Convergence analysis of pressure solutions for the circular inclusion problem with varying density contrast. $\rho_m = 1, \mu_c = 10, \mu_m = 1$.

$\Delta x = \Delta y$	$\rho_c = 2$		$\rho_c = 10$		$\rho_c = 100$		$\rho_c = 1000$	
	$\ e_p\ _\infty$	Order						
1/10	2.61E-2		3.91E-2		5.58E-2		5.69E-2	
1/20	7.06E-3	1.89	1.03E-2	1.92	1.45E-3	1.94	1.48E-2	1.94
1/40	1.98E-3	1.83	2.59E-3	1.75	3.69E-3	1.97	3.73E-3	1.99
1/80	4.72E-4	2.07	6.32E-4	1.97	9.88E-4	1.90	9.97E-4	1.90

indicating that the error in $\Delta \mathbf{u}$ will be transferred into the first-order jump conditions of pressure without amplification. Notice that the scaling factor of D in the definition of $[p]$ does not change with the density contrast, leading to persistent large errors in pressure solution for large viscosity difference. In the simulation with $\mu_c = \mu_m = 2$ and $\rho_c = 10^{-3}$, $\rho_m = 1$, for which

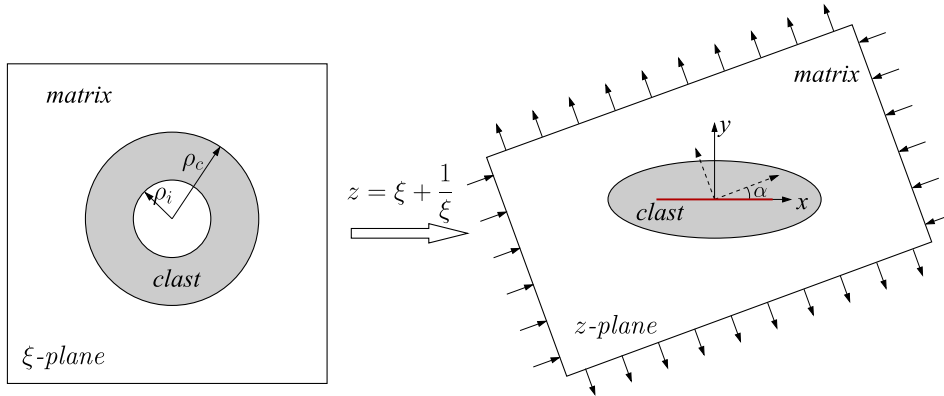


Fig. 7. Illustration of the elliptical inclusion problem and the Joukowski transform. The radius ρ_i of the inner circle of the inclusion in ξ -plane is 1. This circle is mapped onto a slit (red) $-2 \leq x \leq 2$ in the z -plane. α is the angle of incline. (For interpretation of the references to color in this figure legend, the reader is referred to the web version of this article.)

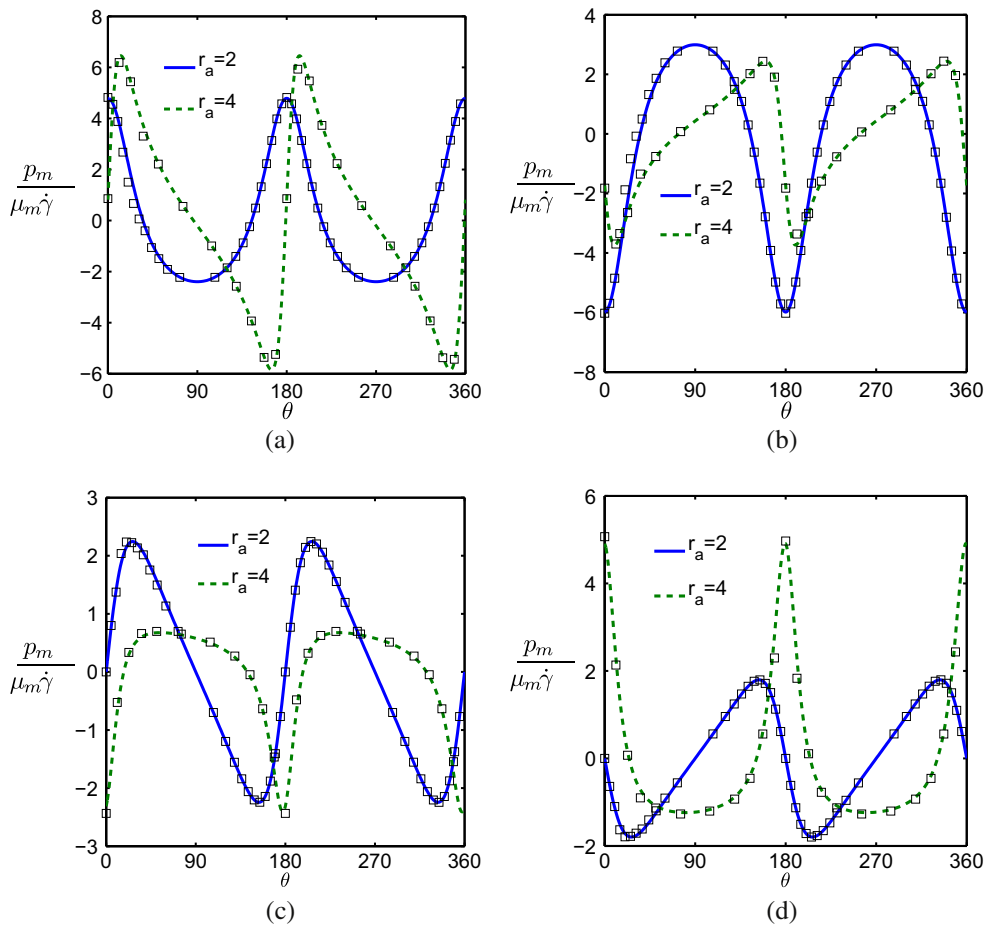


Fig. 8. Matrix pressure at the clast-matrix interface with different elliptical aspect ratio r_a and different viscosity contrast. Lines: analytical values; Markers: Computed values. (a) Ellipse parallel pure shear $\dot{\gamma} = 0$ and $\mu_c = 1/1000$; (b) ellipse parallel pure shear $\dot{\gamma} = 0$ and $\mu_c = 1000$; (c) ellipse parallel simple shear $\dot{\gamma} \neq 0$ and $\mu_c = 1/1000$; (d) ellipse parallel simple shear $\dot{\gamma} \neq 0$ and $\mu_c = 1000$.

the convergence test is not shown here, we again find very large errors in both velocity and pressure, and instability emerges when a smaller ρ_c is used.

Remark 4.1. The exchange of interface conditions is investigated in the context of finite element solutions of the conjugate heat transfer problems with a piecewise heat conductivity [10]. It is shown that error arising from the transfer of the derivative information constitutes an important component in the overall error, and is responsible for the loss of order. However, only moderate contrasts of conductivity are considered in [10] and the instability of the numerical method at large contrasts is not addressed.

4.3. Elliptical inclusion problem

The interests in simulating strong local variations of the stress and pressure fields on the interface motivate us to consider the elliptical inclusion problem. These local variations are hard to simulate with circular inclusion problems because of the built-in angular symmetry. Typical geodynamic processes modeled by elliptical inclusions include deformation in shear zones at high temperature and pressure, wherein the strong clast becomes elongated in the direction sub-parallel to the shear direction [31,45,50]. Fig. 7 illustrates the conformal transformation $z = \xi + 1/\xi$ that maps the inclusion ring in the complex ξ -plane onto the elliptical inclusion with an angle of incline α in the complex z -plane. Application of the Joukowski transform [43] allows one to derive the analytical solutions of the velocity and the pressure fields, which are given as follows:

$$u + iv = \frac{\phi - \left(\xi + \frac{1}{\xi}\right) \overline{\left(\frac{1}{1-\xi^2} \frac{d\phi}{d\xi}\right)} - \bar{\psi}}{2\mu}, \quad (64)$$

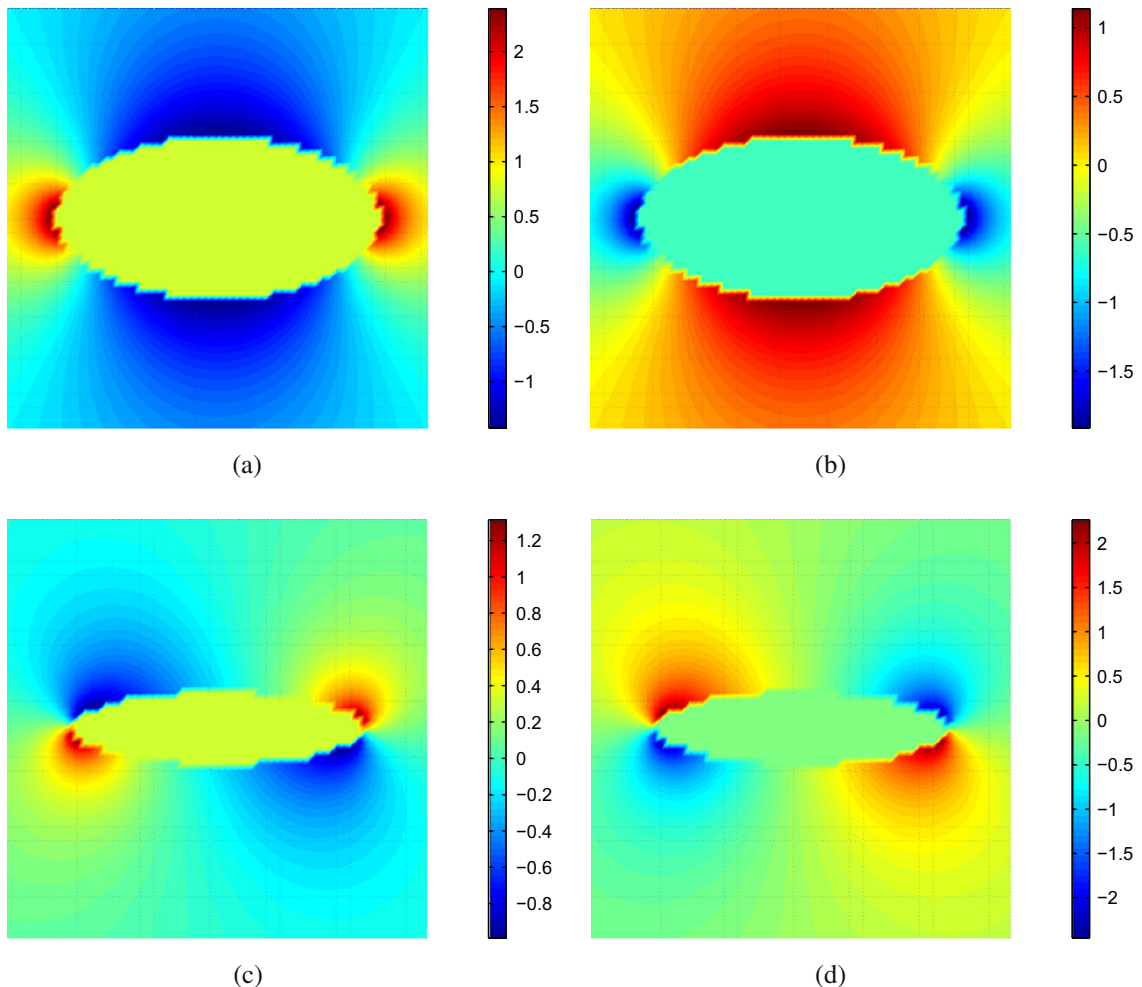


Fig. 9. Pressure field for elliptical inclusion in pure shear: (a) $t=2$, $\dot{\epsilon} = -0.5$, $\alpha = 0^\circ$, $\bar{\mu}_c = 1000$; (b) $t=2$, $\dot{\epsilon} = -0.5$, $\alpha = 0^\circ$, $\bar{\mu}_c = 1/1000$; (c) $t=4$, $\dot{\epsilon} = -0.5$, $\alpha = 0^\circ$, $\bar{\mu}_c = 1000$; (d) $t=4$, $\dot{\epsilon} = -0.5$, $\alpha = 0^\circ$, $\bar{\mu}_c = 1/1000$.

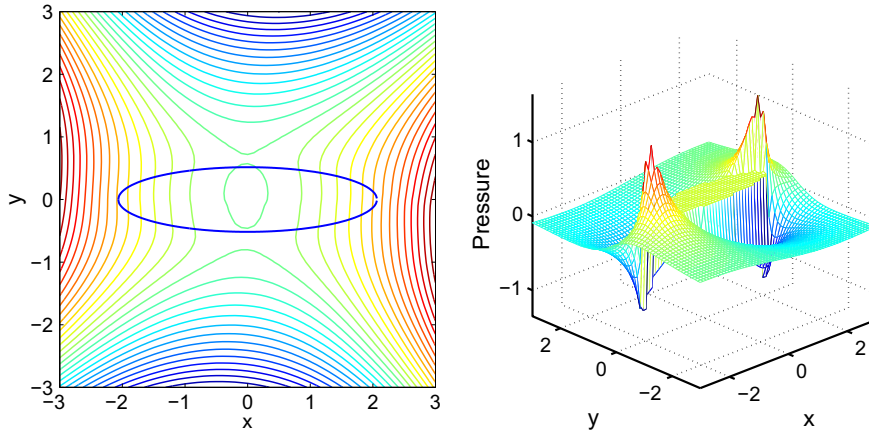


Fig. 10. Stream function (left) and pressure (right) for the case in Fig. 9(d). Sharp change of the pressure on the interface is resolved.

$$p = -2\Re\left(\frac{1}{1-\xi^{-2}} \frac{d\phi}{d\xi}\right), \tag{65}$$

$$\phi_m(\xi) = -\frac{i}{2}\dot{\gamma}\left(\xi + \frac{1}{\xi}\right) + B_3\tilde{\rho}_c^2\left(i\frac{\Im(B)}{B_1} - \frac{\Re(B)}{B_2}\right)\frac{1}{\xi}, \tag{66}$$

$$\psi_m(\xi) = -B\left(\xi + \frac{1}{\xi}\right) + B_5\left(i\frac{\Im(B)}{B_1} - \frac{\Re(B)}{B_2}\right)\frac{1}{\xi^3 - \xi}, \tag{67}$$

$$\phi_c(\xi) = \left\{i\frac{\tilde{\mu}_c B_4 \dot{\gamma}}{2B_1} - \tilde{\rho}_c^2(\tilde{\mu}_c - 1)\left(i\frac{\tilde{\mu}_c \Im(B)}{B_1} - \frac{\Re(B)}{B_2}\right)\right\}\left(\xi + \frac{1}{\xi}\right), \tag{68}$$

$$\psi_c(\xi) = -2\tilde{\mu}_c \tilde{\rho}_c^4 \left(i\frac{\Im(B)}{B_1} + \frac{\Re(B)}{B_2}\right)\left(\xi + \frac{1}{\xi}\right), \tag{69}$$

where $\tilde{\mu}_c$ is μ_c normalized by μ_m , $\tilde{\rho}_c$ is the external radius of the inclusion ring in ξ -plane normalized by the interior radius, and \Im, \Re signify the imaginary and real parts, respectively. The complex number B and the five real constants B_1 through B_5 are defined by

$$\begin{aligned} B &= (2 \cdot \epsilon - i\dot{\gamma})e^{-2i\alpha}, & B_1 &= \tilde{\mu}_c \tilde{\rho}_c^4 + \tilde{\mu}_c + \tilde{\rho}_c^4 - 1, \\ B_2 &= \tilde{\mu}_c \tilde{\rho}_c^4 - \tilde{\mu}_c + \tilde{\rho}_c^4 + 1, & B_3 &= \tilde{\mu}_c \tilde{\rho}_c^4 - \tilde{\mu}_c - \tilde{\rho}_c^4 + 1, \\ B_4 &= -\tilde{\mu}_c \tilde{\rho}_c^4 - \tilde{\mu}_c - \tilde{\rho}_c^4 + 1, & B_5 &= \tilde{\mu}_c \tilde{\rho}_c^8 - \tilde{\mu}_c - \tilde{\rho}_c^4 + 1. \end{aligned}$$

Following the uniqueness of the mapping $\xi(z)$, we can find an inverse mapping $\xi(z)$

$$\xi = \begin{cases} \frac{z + \sqrt{z^2 - 4}}{2}, & \Re(z) \geq 0, \\ \frac{z - \sqrt{z^2 - 4}}{2}, & \Re(z) < 0. \end{cases} \tag{70}$$

We consider the angles $\alpha = 0^\circ$ and two viscosity contrasts $\mu_c/\mu_m = 1000, 1/1000$ with $\mu_m = 1$ and uniform density $\rho_c = \rho_m = 1$. Fig. 8 shows that the computed pressure profiles agree with the analytical solutions very well, and the rapid change of pressure on the interface at $\theta = 0, \pi$ are resolved accurately. In pure shear mode the increase of aspect ratio r_a leads to a larger pressure, while in simple shear mode the inverse is true. It is also observed that the more elongated the elliptical inclusion, i.e., the larger aspect ratio, the larger the pressure gradient at the tips of the inclusion. The complete pressure fields under ellipse-parallel pure shear conditions are plotted in Fig. 9. Comparison between charts (a,c) and charts (b,d) reveals that the pressure field flips when the inclusion changes from strong ($\tilde{\mu}_c = 1000$) to weak ($\tilde{\mu}_c = 1/1000$). Moreover, there is a focusing of the pressure near the tips of the inclusion with increasing aspect ratio c.f. Fig. 9(c) and (d). The focusing does not align with the major axis of the ellipse due to the inclination of the boundary conditions as seen in the stream function plot in Fig. 10.

5. Concluding remarks

Building upon the matched interface and boundary (MIB) approach we have developed a second-order interface method for solving 2D Navier–Stokes equations with discontinuous viscosity and density and fixed interface. A second-order projection method is adopted to ensure the velocity field is divergence free. Starting with the essential interface conditions for the velocity and pressure, we derive the interface conditions for the intermediate velocity and the pressure potential function. These interface conditions are unique for projection methods and have not been explicitly addressed before. We then utilize

the zero and first-order essential interface conditions to get fictitious velocity values that couple both velocity components. Jumps of pressure interface conditions are approximated using the velocity solution. We take advantage of the dimensionally de-coupled first-order pressure (potential) interface conditions so that the fictitious pressure (potential) values can be solved independently along single coordinate directions.

The numerical experiments on time-dependent and steady state problems show that our method has a spatial accuracy of order about 2 for both velocity and the pressure for moderate contrasts of viscosity and for a wide range of density contrasts. The applications to circular and elliptical inclusion problems successfully captures the sharp jumps of the pressure on the interface and the large tangential derivatives along the interface for elongated ellipses. Instability is found for viscosity differences larger than 1000. While similar instability has been attributed to the increase of the condition numbers of the relevant linear systems [49], it is shown here that the appearance of the viscosity difference in the jump of pressure (potential) interface conditions is responsible for the instability encountered for large viscosity difference. This instability results from the amplification of the error in the velocity solution when the pressure (potential) interface conditions are approximated. The amplification can be further complicated with the density contrast in approximating the jumps of pressure (potential) gradients. If the viscosity and density difference are such that $[\mu/\rho] = 1$, the error in velocity derivatives will not be amplified into the pressure (potential) gradients. However, the computed jump $[p]$ is always subjected to a large error for a large viscosity difference regardless of the density contrast. Although higher order interface methods can help postpone the emergence of the instability because of their more accurate approximations of the velocity derivatives on the interface, simulations of large viscosity difference is still challenging, in particular for the extremely large differences found in geodynamic creeping flows. Alternative models that describe the motion of the domain that has a negligible small effective viscosity might help overcome the numerical difficulties associated with very large viscosity differences. Our efforts are currently undertaken to develop such models, and to extend the method to allow for complex shapes at the interfaces such as would naturally develop during creeping geodynamic flows.

Appendix A. Solution Procedure for Fictitious Values along y-Mesh Lines

The final implementable interface conditions for solving fictitious values along y-mesh lines are Eq. (36) or Eq. (37). Below we present the procedure for solving fictitious values $f_{ij}, f_{i,j+1}$ for u and $g_{ij}, g_{i,j+1}$ for v at irregular points $(i,j), (i,j + 1)$ in Fig. 2(b) using interface conditions (36), in which the matrix is denoted by \mathcal{M} . By using the these fictitious values we can approximate the velocity components and their partial derivatives with respect to y at the point of intersection o , as follows:

$$u^- = \sum_{l=i-1}^i P_{0,l}^- u_{lj} + P_{0,i+1}^- f_{i+1,j}, \quad u^+ = P_{0,i}^+ f_{ij} + \sum_{l=i+1}^{i+2} P_{0,l}^+ u_{lj}, \tag{71}$$

$$v^- = \sum_{l=i-1}^i P_{0,l}^- v_{lj} + P_{0,i+1}^- g_{i+1,j}, \quad v^+ = P_{0,i}^+ g_{ij} + \sum_{l=i+1}^{i+2} P_{0,l}^+ v_{lj}, \tag{72}$$

$$u_x^- = \sum_{l=i-1}^i P_{1,l}^- u_{lj} + P_{1,i+1}^- f_{i+1,j}, \quad u_x^+ = P_{1,i}^+ f_{ij} + \sum_{l=i+1}^{i+2} P_{1,l}^+ u_{lj}, \tag{73}$$

$$v_x^- = \sum_{l=i-1}^i P_{1,l}^- v_{lj} + P_{1,i+1}^- g_{i+1,j}, \quad v_x^+ = P_{1,i}^+ g_{ij} + \sum_{l=i+1}^{i+2} P_{1,l}^+ v_{lj}. \tag{74}$$

where $P_{0,l}^\pm$ is the weight at the node (i,l) of the 1D Lagrange interpolant of $u^\pm(x,y)$ at the intersection (x_o, y_o) , and $P_{1,l}^\pm$ is the weight at the node (i,l) of the finite difference approximation to $u_x^\pm(x_o, y_o)$. To approximate x-derivatives, we define auxiliary values $u_1^o, u_2^o, v_1^o, v_2^o$ at the auxiliary nodes (black circles in Fig. 2(b)) to obtain

$$u_x^+ = W_0 u_0 + \sum_{l=1}^2 W_l u_l^o, \quad v_x^+ = W_0 v_0 + \sum_{l=1}^2 W_l v_l^o. \tag{75}$$

The continuity of u, v at the intersection o allows us to replace $u_o = u^-$. By representing the fictitious values in terms of

$$\mathbf{V} = (u_{ij-1}, u_{ij}, u_{ij+1}, u_{ij+2}, u_1^o, u_2^o, v_{ij-1}, v_{ij}, v_{ij+1}, v_{ij+2}, v_1^o, v_2^o, f_\eta)^T$$

such that

$$f_{ij} = \mathbf{C}_1 \cdot \mathbf{V}, \quad f_{i,j+1} = \mathbf{C}_2 \cdot \mathbf{V}, \quad g_{ij} = \mathbf{C}_3 \cdot \mathbf{V}, \quad g_{i,j+1} = \mathbf{C}_4 \cdot \mathbf{V},$$

we can summarize the approximation to the four interface conditions (71)–(74) as

$$\mathcal{M} \begin{pmatrix} \mathbf{C}_1 \\ \mathbf{C}_2 \\ \mathbf{C}_3 \\ \mathbf{C}_4 \end{pmatrix} \mathbf{V} = \mathbf{E}. \tag{76}$$

Here

$$\mathcal{M} = \begin{pmatrix} P_{0j}^+ & -P_{0j+1}^- & 0 & 0 \\ 0 & 0 & P_{0j}^+ & -P_{0j+1}^- \\ M_{12}P_{1j}^+ & (M_{11} + M_{15}W_0)P_{1j+1}^- & M_{14}P_{1j}^+ & (M_{13} + M_{16}W_0)P_{1j+1}^- \\ M_{22}P_{1j}^+ & (M_{21} + M_{25}W_0)P_{1j+1}^- & M_{24}P_{1j}^+ & (M_{23} + M_{26}W_0)P_{1j+1}^- \end{pmatrix},$$

and

$$\begin{aligned} E_1 &= \sum_{l=j-1}^j P_{0,l}^- u_{i,l} - \sum_{l=j+1}^{j+2} P_{0,l}^+ u_{i,l}, & E_2 &= \sum_{l=j-1}^j P_{0,l}^- v_{i,l} - \sum_{l=j+1}^{j+2} P_{0,l}^+ v_{i,l}, \\ E_3 &= - \sum_{l=j-1}^j P_{1,l}^- (M_{11} + M_{15}W_0) u_{l,j} - \sum_{l=j-1}^j P_{1,l}^- (M_{13} + M_{16}W_0) v_{l,j} \\ &\quad - \sum_{l=i+1}^{i+2} P_{1,l}^+ (M_{12}u_{l,j} + M_{14}v_{l,j}) - M_{15} \sum_{l=1}^2 W_l u_l^0 - M_{16} \sum_{l=1}^2 W_l v_l^0, \\ E_4 &= - \sum_{l=j-1}^j P_{1,l}^- (M_{21} + M_{25}W_0) u_{l,j} - \sum_{l=j-1}^j P_{1,l}^- (M_{23} + M_{26}W_0) v_{l,j} \\ &\quad - \sum_{l=j+1}^{j+2} P_{1,l}^+ (M_{22}u_{l,j} + M_{24}v_{l,j}) - M_{25} \sum_{l=1}^2 W_l u_l^0 - M_{26} \sum_{l=1}^2 W_l v_l^0 + f_{\eta}. \end{aligned}$$

Define matrix \mathbf{B} so that $\mathbf{E} = \mathbf{B}\mathbf{V}$. We can solve for the four sets of expansion coefficients

$$\mathbf{C} = \mathcal{M}^{-1}\mathbf{B}.$$

References

- [1] D.L. Anderson, R.S. Hart, An earth model based on free oscillations and body waves, *J. Geophys. Res.* 81 (1976) 1461–1475.
- [2] D.L. Anderson, J.B. Minster, The frequency dependence of Q in the earth and implications for mantle rheology and Chandler wobble, *Geophys. J. R. Astr. S.* 58 (1979) 431–440.
- [3] P.J. Atzberger, P.R. Kramer, C.S. Peskin, A stochastic immersed boundary method for fluid–structure dynamics at microscopic length scales, *J. Comput. Phys.* 224 (2007) 1255–1292.
- [4] D.L. Brown, R. Cortez, M.L. Minion, Accurate projection methods for the incompressible Navier–Stokes equations, *J. Comput. Phys.* 168 (2001) 464–499.
- [5] P.H. Chiu, R.K. Lin, Tony W.H. Sheu, A differentially interpolated direct forcing immersed boundary method for predicting incompressible Navier–Stokes equations in time-varying complex geometries, *J. Comput. Phys.* 229 (12) (2010) 4476–4500.
- [6] P.N. Chopra, M.S. Paterson, The experimental deformation of dunite, *Tectonophysics* 78 (1981) 453–473.
- [7] G.F. Davies, M.A. Richards, Mantle convection, *J. Geol.* 100 (1992) 151–206.
- [8] Y. Deubelbeiss, B.J.P. Kaus, Comparison of Eulerian and Lagrangian numerical techniques for the Stokes equations in the presence of strongly varying viscosity, *Phys. Earth Planet. In.* 171 (2008) 92–111.
- [9] A.M. Dziewonski, A.L. Hales, E.R. Lapwood, Parametrically simple earth models consistent with geophysical data, *Phys. Earth Planet. In.* 10 (1975) 12–48.
- [10] D. Estep, S. Tavener, T. Wildey, A posteriori analysis and improved accuracy for an operator decomposition solution of a conjugate heat transfer problem, *SIAM J. Numer. Anal.* 46 (2008) 2068–2089.
- [11] R.E. Ewing, Z. Li, T. Lin, Y. Lin, The immersed finite volume element method for the elliptic interface problems, *Math. Comput. Simul.* 50 (1999) 63–76.
- [12] R. Fedkiw, T. Aslam, B. Merriman, S. Osher, Non-oscillatory Eulerian approach to interfaces in multimaterial flows (the ghost fluid method), *J. Comput. Phys.* 152 (1999) 457–492.
- [13] R. Fedkiw, X.D. Liu, The ghost fluid method for viscous flows, in: *Innovative Methods for Numerical Solutions of Partial Differential Equations*, World Scientific Publishing, 2002.
- [14] Gale. <<http://www.geodynamics.org/cig/software/gale>>.
- [15] R.S. Hart, D.L. Anderson, H. Kanamori, The effect of attenuation on gross earth models, *J. Geophys. Res.* 82 (1977) 1647–1654.
- [16] S. Hou, X.-D. Liu, A numerical method for solving variable coefficient elliptic equation with interfaces, *J. Comput. Phys.* 202 (2005) 411–445.
- [17] S. Hou, L. Wang, W. Wang, Numerical method for solving matrix coefficient elliptic equation with sharp-edged interfaces, *J. Comput. Phys.* 229 (2010) 7162–7179.
- [18] Myungjoo Kang, Ronald P. Fedkiw, X.-D. Liu, A boundary condition capturing method for multiphase incompressible flow, *J. Sci. Comput.* 15 (3) (2000) 323–360.
- [19] S. Karato, Rheology of the lower mantle, *Phys. Earth Planet. In.* 24 (1981) 1–14.
- [20] B.J.P. Kaus, Numerical Modelling of Geodynamical Instabilities, Ph.D. Thesis, ETH Zurich, 2004.
- [21] J. Korenaga, T.H. Jordan, Physics of multiscale convection in Earth's mantle: evolution of sublithospheric convection, *J. Geophys. Res.* 109 (2004).
- [22] D.V. Le, B.C. Khoo, J. Peraire, An immersed interface method for viscous incompressible flows involving rigid and flexible boundaries, *J. Comput. Phys.* 220 (2006) 109–138.
- [23] J. LeVeque, Zhilin Li, The immersed interface method for elliptic equations with discontinuous coefficients and singular sources, *SIAM J. Numer. Anal.* 31 (1994) 1019–1041.
- [24] Z. Li, K. Ito, *The Immersed Interface Method: Numerical Solutions of PDEs Involving Interfaces and Irregular Domains*, SIAM, 2006.
- [25] Zhilin Li, The immersed interface method using a finite element formulation, *Appl. Numer. Math.* 27 (3) (1998) 253–267.
- [26] Zhilin Li, Ming-Chih Lai, The immersed interface method for the Navier–Stokes equations with singular forces, *J. Comput. Phys.* 171 (2001) 822–842.
- [27] Zhilin Li, Tao Lin, Xiaohui Wu, New cartesian grid methods for interface problems using the finite element formulation, *Numer. Math.* 96 (2003) 61–98.
- [28] L. Moresi, V. Solomatov, Numerical investigations of 2D convection in a fluid with extremely large viscosity variations, *Phys. Fluids* 7 (1995) 2154–2162.

- [29] L. Moresi, S.J. Zhong, M. Gurnis, The accuracy of finite element solutions of Stokes flow with strongly varying viscosity, *Phys. Earth Planet. In.* 97 (1996) 83–94.
- [30] L.F. Moresi, F. Dufour, H.-B. Mulhaus, Mantle convection modeling with viscoelastic/brittle lithosphere: numerical methodology and plate tectonic modeling, *Pure Appl. Geophys.* 159 (2002) 2335–2356.
- [31] J.K. Morgan, M.S. Boettcher, Numerical simulations of granular shear zones using the distinct element method. 1. Shear zone kinematics and the micromechanics of localization, *J. Geophys. Res.* 104 (1999) 2703–2719.
- [32] J. Moser, C. Matyska, D.A. Yuen, A.V. Malevsky, H. Harder, Mantle rheology, convection, and rotational dynamics, *Phys. Earth Planet. In.* 79 (1993) 367–381.
- [33] R.J. O'Connell, On the scale of mantle convection, *Tectonophysics* 38 (1977) 119–136.
- [34] M. Oevermann, C. Scharfenberg, R. Klein, A sharp interface finite volume method for elliptic equations on cartesian grids, *J. Comput. Phys.* 228 (14) (2009) 5184–5206.
- [35] C.S. Peskin, Numerical analysis of blood flow in the heart, *J. Comput. Phys.* 25 (1977) 220–252.
- [36] C.S. Peskin, The immersed boundary method, *Acta Numer.* 11 (2002) 479–517.
- [37] G. Ranalli, *Rheology of the Earth*, Chapman and Hall, 1995.
- [38] G. Ranalli, B. Fischer, Diffusion creep, dislocation creep, and mantle rheology, *Phys. Earth Planet. In.* 34 (1984) 77–84.
- [39] G. Ranalli, D.C. Murphy, Rheological stratification of the lithosphere, *Tectonophysics* 132 (1987) 281–295.
- [40] F. M. Richter, B. Parsons, On the interaction of two scales of convection in the mantle, *J. Geophys. Res.* 80 (1975) 2529–2541.
- [41] S.M. Schmalholz, Y.Y. Podladchikov, D.W. Schmid, A spectral/finite difference method for simulating large deformations of heterogeneous, viscoelastic materials, *Geophys. J. Int.* 145 (2001) 199–208.
- [42] D.W. Schmid, *Finite and Infinite Heterogeneities Under Pure and Simple Shear*, Ph.D. Thesis, Swiss Federal Institute of Technology, 2002.
- [43] Daniel W. Schmid, Yuri Yu. Podladchikov, Analytical solutions for deformable elliptical inclusions in general shear, *Geophys. J. Int.* 155 (2003) 269–288.
- [44] Daniel W. Schmid, Yuri Yu. Podladchikov, Are isolated stable rigid clasts in shear zones equivalent to voids?, *Tectonophysics* 384 (1–4) (2004) 233–242.
- [45] Carol Simpson, Declan G. De Paor, Strain and kinematic analysis in general shear zones, *J. Struct. Geol.* 15 (1) (1993) 1–20.
- [46] X.D. Song, P.G. Richards, Seismological evidence for differential rotation of the earth's inner core, *Nature*. 382 (1996) 221–224.
- [47] E. Tan, E. Choi, P. Thoutireddy, M. Gurnis, M. Aivazis, Geoframework: Coupling multiple models of mantle convection within a computational framework, *Geochem. Geophys. Geosyst.* 7 (2006) Q06001.
- [48] Zhijun Tan, D.V. Le, K.M. Lim, B.C. Khoo, An immersed interface method for the incompressible Navier–Stokes equations with discontinuous viscosity across the interface, *SIAM J. Sci. Comput.* 31 (2009) 1798–1819.
- [49] Zhijun Tan, D.V. Le, Zhilin Li, K.M. Lim, B.C. Khoo, An immersed interface method for solving incompressible viscous flows with piecewise constant viscosity across a moving elastic membrane, *J. Comput. Phys.* 227 (2008) 9955–9983.
- [50] Basil Tikoff, David Greene, Stretching lineations in transpressional shear zones: an example from the Sierra Nevada Batholith, California, *J. Struct. Geol.* 19 (1) (1997) 29–39.
- [51] M.C. Tsenn, N.L. Carter, Upper limits of power law creep of rocks, *Tectonophysics* 136 (1987) 1–26.
- [52] Oleg V. Vasilyev, Yuri Yu. Podladchikov, David A. Yuen, Modeling of viscoelastic plume–lithosphere interaction using adaptive multilevel wavelet collocation method, *Geophys. J. Int.* 147 (2001) 579–589.
- [53] Wei-Cheng Wang, A jump condition capturing finite difference scheme for elliptic interface problems, *SIAM J. Numer. Anal.* 25 (2004) 1479–1496.
- [54] J. Weertman, Creep laws for the mantle of the earth, *Philos. Trans. R. Soc. Lond. A* 288 (1978) 9–26.
- [55] S. Xu, Derivation of principal jump conditions for the immersed interface method in two-fluid flow simulation, *Discret. Contin. Dyn. S.* (2009) 838–845.
- [56] S. Xu, Z. Jane Wang, Systematic derivation of jump conditions for the immersed interface method in three-dimensional flow simulation, *SIAM J. Sci. Comput.* 27 (2006) 1948–1980.
- [57] Sining Yu, Y.C. Zhou, G.W. Wei, Matched interface and boundary (mib) method for elliptic problems with sharp-edged interfaces, *J. Comput. Phys.* 224 (2007) 729–756.
- [58] S. Zhang, D.A. Yuen, The influences of lower mantle viscosity stratification on 3d spherical-shell mantle convection, *Earth Planet. Sci. Lett.* 132 (1995) 157–166.
- [59] S. Zhao, G.W. Wei, High order FDTD methods via derivative matching for Maxwell's equations with material interfaces, *J. Comput. Phys.* 200 (2004).
- [60] S.J. Zhong, D.A. Yuen, L.N. Moresi, Numerical methods for mantle convection, in: *Treatise on Geophysics, Mantle Dynamics*, Vol. 7, Elsevier, 2007.
- [61] S.J. Zhong, M.T. Zuber, L. Moresi, M. Gurnis, Role of temperature-dependent viscosity and surface plates in spherical shell models of mantle convection, *J. Geophys. Res.* 105 (2000) 111063–111082.
- [62] Y.C. Zhou, G.W. Wei, On the fictitious-domain and interpolation formulations of the matched interface and boundary (MIB) method, *J. Comput. Phys.* 219 (2006) 228–246.
- [63] Y.C. Zhou, Shan Zhao, Michael Feig, G.W. Wei, High order matched interface and boundary (MIB) schemes for elliptic equations with discontinuous coefficients and singular sources, *J. Comput. Phys.* 213 (2006) 1–30.